Chapter 3
Nanomaterials: Basic Concepts and Quantum Models

Maura Cesaria and Baldassare Di Bartolo

Abstract The term "nanosystem" refers to a system with at least one spatial dimension scaled down to the nanometer-scale (<100 nm) and includes zero-dimensional systems (such as metallic, semiconducting and ceramic nanoparticles), one-dimensional systems (such as nanowires, nanotubes and nanorods) and two-dimensional structures (thin films or plates).

The fascinating properties of materials at the nanoscale are continuing to attract the scientific interest in many research fields at both applicative and fundamental levels. The impossible to comprehensively review large number of reports and results available in the literature demonstrates the complexity in describing all the functionalities offered by the nanosystems as well as their properties as related to their fabrication approaches apart from departure from bulk form. To be able to gain insight into the potentialities and new future perspectives offered by the nanoworld and nanotechnology, knowledge and understanding of the physical fundamentals is a necessary starting point.

In this review paper, we consider and discuss the spectroscopy of nanomaterials by pointing out differences and breaking points as compared to the bulk counterparts, the importance of the surfaces, the characteristic length-scales (De Broglie wavelength, Fermi wavelength and exciton Bohr radius) that define various confinement regimes, the physics underlying the formalism to calculate the electronic dispersion of the low-dimensionality systems and the technological benefits on the excitonic binding energy implied by low-dimensionality (zero-, one- and two-dimensionaity). The presented discussion aims at laying a foundation to further studies for a reader new to the field of nanomaterials.

M. Cesaria
Department of Mathematics and Physics "Ennio De Giorgi", University of Salento, Lecce, Italy
e-mail: maura.cesaria@le.infn.it

B. Di Bartolo (✉)
Department of Physics, Boston College, Chestnut Hill, MA, USA
e-mail: dibartob@bc.edu

3.1 Introduction

The nomenclature "nanomaterials" refers to materials with at least one dimension in the nanometer (1 nm $= 10^{-9}$ m) range (from 1 to 100 nanometers) that are commonly classified as zero-dimensional (0D), one-dimensional (1D) and two-dimensional (2D) structures. In general, adding one more confinement direction can affects the system properties remarkably and involve different applications. In practice, the systems of interest in nano-science are more often composed of ensembles of nanostructures instead of single nanostructures because of processing. Hence, on one hand, fabrication processes able to control such dispersion are critical and, on the other hand, dispersion in size and shape must be taken into account to interpret the experimental findings and to design devices exploiting the properties at the nanoscale.

The first lecture (titled "There's Plenty of Room at the Bottom") regarding possible applications for nanomaterials dates to 1959 and was given by the Physics Nobel Laureate (in 1965) Richard Feynman at the annual American Physical Society meeting on the campus of Caltech [1]. The challenging concept expressed by Feynman in this seminal lecture was miniaturization as a possibility to collect/encode a huge amount of information in increasingly small spaces. Even if no practical way to accomplish all of this was known then, this idea laid the conceptual foundations for applications exploiting very short length-scales and new properties of materials. In this sense, Feynman challenged scientists to collaborate and explore increasingly small sizes and the applicative perspectives in this realm without thinking small about the solution of future challenging problems. In 1984 Feynman was invited to give an updated version of his landmark lecture at a weeklong seminar held at the Esalen Institute. His talk, titled "Tiny Machines", while discussing the important technological advances since 1954, demonstrated that his first outlined picture of nanoworld was prescient and farsighted.

Over the years, there has been a growing widespread interest in nanomaterials (also termed mesoscopic systems) at both fundamental and applicative level leading to a new promising research field named "nanotechnology". This term was first introduced in 1974 by Norio Taniguchi at the International Conference on Precision Engineering (ICPE) [2] and refers to processes enabling to engineer and fabricate objects with control on the nanoscale level.

The development of nanoscience demands fundamental knowledge of the physical properties at the nanoscale level and new technologies both in fabrication processes and investigation tools as well as interaction/exchange of various research fields including physics, chemistry, material science and engineering, just as previewed by Feynman. Efforts of fundamental research are presently focused on understanding the origin of the mechanical, chemical, reactivity, catalysis, thermal, electrical, optical, and magnetic properties of nanomaterials, which strongly differ from the ones of the large-scale structures of the same composition (i.e., bulk counterpart). Changes of the bulk properties involved by size-effects can be observed as regards

- chemical properties: reactivity and catalysis
- thermal properties: melting temperature and thermal conduction
- mechanical properties: adhesion and capillary forces
- optical properties: band-structure, absorption and scattering
- electrical properties: Coulomb charging, quantized conductance, quantum tunneling current
- magnetic properties: superparamagnetic effect

On the other hand, technology aims at engineering and controlling nanomaterial shape and size, size- and shape- dispersion and composition. Hence, since investigation of the nanoworld and nanotechnology takes advantage from imaging, measuring, modeling and manipulating matter at the nanometer scale, powerful observation tools, such as electron microscopes (scanning electron microscope (SEM) and transmission electron microscope (TEM)) [3–6], scanning-tunneling microscope (STM) [7, 8], atomic force microscope (AFM) [9] and scanning near-field optical spectroscopy (SNOM) [10, 11] were decisive in enabling and prompting progress in the nanoscale field. STM uses a sharp metal tip brought close (0.3÷1 nm) to the surface to be investigated to measure a detectable electron tunneling current. The "tunneling" of electrons (quantum tunneling effect) between the tip and the substance creates a current (flow of electrons) that lets acquire an image of the sample by changing the current intensity over the time. The reachable resolution (0.1 ÷1 nm) enables to observe even single atoms. Today's STMs allow not only to see atoms but also to measure the electronic density of states of single nanostructures as well as to move atoms around and arrange them in a specific designed configuration. Whereas STM works only on electrically conductive samples, AFM can image the surface of any (inorganic, organic, conductive and insulator) material with such a high resolution to define the position of individual atoms. The working principle of AFM can be summarized as follows. A tiny tip at the end of a flexible micro-cantilever is scanned in a raster pattern over the surface to be imaged by a piezoelectric actuator with sub-Angstrom accuracy. Cantilever deflection results from the tip-sample (short-range chemical binding, van-der Waals, electrostatic or magnetic) interaction which is kept to a fixed value by a feedback circuit in almost all operating modes of the AFM instrument. The cantilever deflection is carefully monitored by a laser beam reflected off the back of the cantilever towards a four-quadrant split position-sensitive photodetector acting as amplifier of the cantilever deflection.

Near-field optical probing (SNOM) enables to image and measure the optical properties of single semiconductor quantum nano-structures, even distributed at a spatial density of the order of $100/\mu m^2$, with spatial subnanometer resolutions, i.e., well beyond the diffraction limit of light. Conventional optical microscopes obtain the image of an object without being able to gain information about fine (subwavelength) features due to the diffraction limit [12], meaning that detail can't be greater than 0.61 λ/NA where λ is the probing wavelength and NA is the numerical aperture of the microscope optics. To overcome the limits of conventional microscopes the sample should be illuminated by a small aperture with diameter

d much shorter than the probing wavelength and at a distance much shorter than d from the surface to be imaged (near-field region). SNOM technology exploits a tapered optical fiber with a metalized terminal part having diameter d of a few tens of nanometers and enables to collect local emission from the surface region just underneath the microscope aperture. Since a few hundreds of nW of laser light shine the sample, a high collection efficiency is a prerequisite to be able to detect very low level photoluminescence signals by SNOM spectroscopy.

Undoubtedly, nanotechnology would not exist without the above mentioned powerful tools and many fascinating properties of mesoscopic systems would never have been disclosed. In this respect, while the fundamental behavior of bulk materials is inherently determined by structure and composition, at the nanometer length-scale peculiar phenomena occur strictly related to either spatial confinement of the electronic as well as phonon wave-functions or surface-effects. For example, as it will be thoroughly discussed later, when at least one length (L) of a semiconductor system along a spatial direction is comparable with a characteristic length-scale (the so-called De Broglie electronic wavelength of the corresponding bulk material), then the energy spectrum becomes quantized along the confinement direction. Such phenomenon, termed "quantum size effect", involves a larger band gap and a blue shift of the absorption onset with decreasing size as compared to the bulk counterpart, meaning that the optical properties of a nanostructure are tunable as a function of both the confinement length L and number of the confinement directions (0D, 1D and 2D nanostructures).

A further consequence of low-dimensional confinement is the increase of the binding energy of an exciton (i.e., an electron-hole pair bounded by the Coulomb interaction) resulting from the enhanced Coulomb coupling between electrons and holes achievable by carrier localization in a nanostructure. This low-dimensional effect is a prerequisite to be able to observe excitonic effects in semiconductor mesoscopic systems working at room temperature and exploiting optical non-linearity in optoelectronic devices.

Moreover, discrete phonon density of states is characteristic of the nanoscale [13] and low-frequency acoustic phonon modes are cut off depending on the nanostructure size [14–17].

Since electron-phonon interaction determines the thermal conductivity and affects carrier dynamics in quantum-confined systems, different thermalization rules and processes (multiphonon processes [18, 19], Coulomb interactions and phonon-bottleneck effects [20, 21]) have to be considered in the nanoworld.

Turning to metal nanoclusters/nanoparticles, for which there is no band-gap, another nanoparticle phenomenon, known as *plasmon resonance*, is active that results from the resonant oscillation of surface conduction electrons stimulated by incident light with the plasma wavelength [22–29]. Scaling down to dimensions of a few nanometers, surface plasmon resonance disappears in metal nanostructures. In fact, as the spacings between adjacent energy levels (referred to as the Kubo gap) become comparable to the thermal energy $k_B T$ (where k_B is the Boltzmann constant and T the absolute temperature), a shift in conductive properties, from metallic to semiconducting and insulating, results for decreasing size [30–32].

Metallic nanoparticles have a huge potential in nanotechnology thanks to optimized synthesis approaches enabling control on their size, shape and degree of aggregation. Under resonant excitation, an enhancement of the local electric fields close to the metal nanoparticle surface occurs that is the basis of important applications such as surface-enhanced Raman Spectroscopy (SERS) [26, 33–35]. Such an active recent research field uses various chemical functional groups favoring bonds/interactions with antibodies, ligands, and drugs of interest in biotechnology, nano-medicine and diagnostic imaging. Furthermore, other applications exploit metal nanoparticles with modified composition and core-shell structure [36]. Metal nanoparticles are also interesting for sensor applications and enhanced catalytic activity involved by increased fraction of surface atoms and surface curvature with decreasing size as well as particle-particle and particle-chemical interactions [37].

Also, surface effects are responsible for fundamentally and technologically important experimental findings such as pre-melting (i.e., melting initiated at the surface) and size-dependent depression of the melting temperature (i.e., lowered melting temperature as compared to the bulk counterpart) [38–46].

A further amazing phenomenon peculiar of the nanoworld is the substantial increment of the thermal conductivity exhibited by nanofluids (very low concentrations of nanostructures dispersed in solvents with suitable relative thermal conductivity) which varies with size, shape, and material of the nanostructures as well as difference of thermal conductivity between bulk material and base fluid [47].

On the other hand, the evidence of quantum size effects makes the Planck's black-body model unable to describe the thermal emission spectrum at the nanoscale (at particle dimensions smaller than the radiation wavelength), where the Stefan–Boltzmann law yields strongly overestimated results [48–50]. Moreover, nanoworld also involves magnetic properties different as compared to the bulk materials [51, 52].

Extensive, even if not exhaustive because of continuous progress and developments, literature is available about nanoscience (nanomaterials and nanotechnology) and a comprehensive review of the existing scenario is outside the scope of this paper. The subject of quantum-confined structures is wide, in continuous progress and involves fundamental quantum mechanical models, applications in different fields and processing of materials and architectures at the nanoscale.

Instead, in the following we overview and critically discuss the spectroscopic properties of nanomaterials at the fundamental level with a focus on the underlying physics and breaking points with respect to the bulk counterparts. We aim at introducing a beginner reader to the fascinating world of low-dimensional systems from the fundamental standpoint, i.e., accounting for the understanding of low-dimensional physics as a tool for gaining insight in the potentialities and future perspectives of the nanoworld. In this perspective, we consider the surface-related effects (increased surface-to volume ratio (SVR) and the related modified chemistry and thermal stability of nanomaterials) and their technological importance while scaling down dimensions to the nanoscale level. Furthermore we overview and discuss basic concepts such as optical confinement characteristic lengths (De

Broglie wavelength, Fermi wavelength and exciton Bohr radius), the meaning of the classification-scheme of low-dimensionality systems (zero-, one- and two-dimensional systems), quantum mechanical models to mathematically describe the electronic structure and quantum size effects in semiconductor nanostructures as well as excitons in nanostructures, and the size-induced dramatic changes of the electronic dispersion of metallic nanostructures.

3.2 Basic Concepts Underlying Nanoscience

Nanoscience deals with phenomena and processing involving systems with nanometer dimensions (termed nanostructures or low-dimensional structures or mesoscopic structures). Drastic (from macroscopic to nanometer-scale) reduction in size results in physicochemical (electrical, mechanical, chemical, thermal, magnetic, and optical) properties that remarkably depart from the ones of the bulk counterpart whenever a characteristic dimension becomes comparable with some fundamental length-scale of the material. In this regime, the spatial confinement involves changes of the electronic dispersion, usually falling into the category of quantum-size effects, that can be detected in the optical response of nanostructures and lead to new device performances and technologies. Nanoscale spectroscopy is not only size-dependent but can also be controlled by the number of confinement dimensions (i.e. shape of the nanostructure) leading to atom-like spectrum when the confinement occurs in all directions (zero-dimensional structure or quantum dot or nanoparticle). At the nanoscale, tuning of size and shape also affects the surface energy: the smaller the nanostructure and the larger the number of edges, the larger is the contribution of the surface energy, a fact which decreases the cohesive energy. Since the cohesive energy dominates phenomena such as melting, evaporation and phase transition, scaling down to nanometer size involves modified thermal stability as compared to the bulk case. All of this has very interesting fundamental and applicative perspectives that will be examined.

In the present section of our paper we introduce the reader to nomenclature and basic concepts in nanoscience such as characteristic length-scales in solids (De Broglie wavelength, exciton Bohr radius and Fermi wavelength), their interplay with confinement effects leading to the classification of the mesoscopic systems as 2D-, 1D- and 0D-dimensional systems, size-induced (quantum-size effect) and surface-related effects.

3.2.1 Characteristic Scale-Lengths in Bulk Solids

The regimes where the properties of materials became size- and shape-dependent are defined by a set of characteristic length scales and their relationship with the physical dimensions of the system. In the following we briefly overview the basic

concepts of the solid state physics enabling to introduce such relevant length scales (i.e., De Broglie wavelength and exciton Bohr radius in semiconductors, and Fermi wavelength in metals).

In the framework of the solid state theory a simple model, the so-called free-electron model, is often applied to solve for the Scroedinger equation of atomic and metal systems. Such a model assumes independent and free electrons obeying the Pauli-exclusion principle (Fermi-Dirac distribution function). To calculate systems described by a periodic potential (semiconductor crystals), it has been modified to include corrections to the pure free-electron model accounted for the band-structure and carriers' effective mass [53].

Based on the solid state physics [53], materials with ordered (periodic) lattice structure can exhibit electronic energy dispersion organized according alternate bands of allowed and forbidden energies. The highest fully occupied band and the lowest empty or partially occupied band are termed valence band and conduction band, respectively, and are separated by a continuum of electronic forbidden energies referred to as energy band-gap (Fig. 3.1). The width of such a band-gap (E_g) as compared to the thermal energy k_BT is of interest to classify materials as insulators or semiconductors. In fact, when in the ground state (zero absolute temperature, $T = 0$ K) E_g is much too wide to allow electrons from the valence band to be thermally promoted to the conduction band at room temperature ($k_BT \approx 25$ meV at $T = 300$ K) then a material is classified as insulator. In this case the valence band (and all bands of lower energy) is fully occupied, and the conduction band is empty (implying vanishing conductivity) even at temperature almost higher than the room temperature. Instead, a semiconductor material is insulator at $T = 0$ K but its energy band-gap smaller compared to insulators (~a few eV) enables the conduction band to be thermally populated around its minimum at room temperature, which implies electric conductivity. In addition to insulators and semiconductors, important materials in condensed matter physics are metals that do not have forbidden energy gap, i.e., at $T = 0$ K their conduction electrons occupy
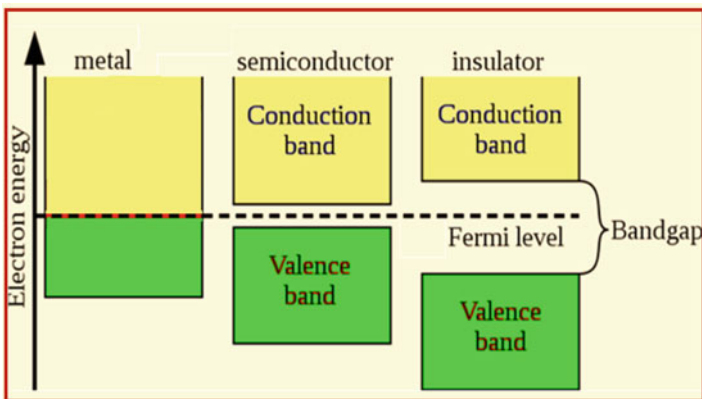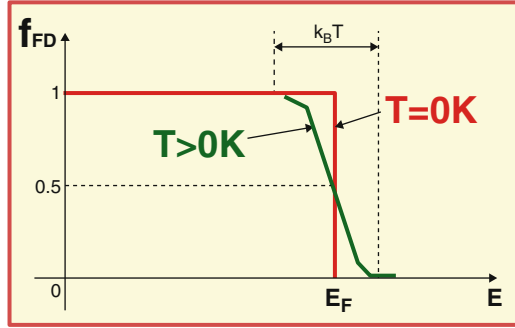

Fig. 3.1 Schematics of the band structure of a metal, semiconductor and insulator material

Fig. 3.2 Fermi-Dirac distribution function

a continuum of energy levels (the so-called "Fermi sphere") with maximum energy corresponding to the so-called "Fermi energy"(E_F). In metals the allowed electronic states with energy higher than E_F are depopulated at $T = 0$ K and can be thermally populated at any non-vanishing low temperature due to the absence of a forbidden energy gap. In general, E_F is defined as the highest energy level below which all electronic energy levels are filled and above which all electronic energy levels are empty at $T = 0$ K. In terms of statistics, E_F is defined by the Fermi-Dirac statistics which describes the probability density that fermions (like electrons) can occupy an allowed state at energy E as a function of the temperature (Fig. 3.2). Being T the absolute temperature, the Fermi-Dirac distribution function f_{FD} has the following mathematical expression:

$$f_{FD}(E, T) = \left(1 + e^{\frac{-(E-\mu)}{k_B T}} \right)^{-1}$$

where k_B is the Boltzmann's constant and μ is the so-called "total chemical potential" (tending to E_F at $T = 0$ K). Based on the Fermi-Dirac statistics, it results $f_{FD}(E_F, T = 0$ K$) = 1/2$, i.e., the probability of occupation at E_F is 1/2. Notably, E_F is the ground state ($T = 0$ K) limit of the chemical potential μ and may be or may not be an electronic allowed energy. In fact, while in metals E_F is the maximum occupied electronic energy, in semiconductors and insulators E_F is located in the middle of the forbidden band-gap (Fig. 3.1), consistently with fully occupied valence band and empty conduction band in the ground state ($T = 0$ K). At $T > 0$ K the step-like profile of f_{FD} at $T = 0$ K smooths/rounds and a tail develops extending towards $E > E_F$ with $f_{FD}(\mu, T) = 1/2$ (Fig. 3.2) at any $T > 0$ K. The chemical potential μ shifts with temperature as well as doping content and type (*n*-type or *p*-type).

Another important difference between band-gap materials and metals is the nature of carriers, i.e. electrons in metals and both electrons and holes in semi-conductors. The concept of hole is introduced to account for the properties of the missing electron in the valence band.

The outlined background of solid state physics provides the basic information necessary to introduce and discuss characteristic length scales in solids.

In semiconductors, the characteristic length scale of carriers (electrons and holes) is the De Broglie wavelength λ_{DB} given by

$$\lambda_{DB} = h/p$$

where $\mathbf{p} = m^* \mathbf{v}$ is the momentum of a carrier with effective mass m* (determined by the crystal lattice) and velocity $\mathbf{v}$ and $h = 6.62 \times 10^{-34}$ Js is the Planck's constant. In general, holes have larger effective mass and lower velocity than electrons in a given material. For example, in GaAs, the effective mass of electrons and holes and their thermal velocity are given by $m_e^* = 0.063\ m_o$, $m_h^* = 0.53\ m_o$, $\mathbf{v}_e = 4.4 \cdot 10^5$ m/s and $\mathbf{v}_h = 1.8 \cdot 10^5$ m/s. Based on the definition, after substituting $h = 6.62 \times 10^{-34}$ Js and $1\ J = 1$ kg m^2/s^2, the De Broglie wavelength can be expressed as $\lambda_{DB} = (727 \times 10^3$ nm$)/(m^*/m_o)v$, where m^*/m_o is the carrier effective mass expressed in units of m_o ($m_o = 9.11 \times 10^{-31}$ Kg, mass of a free electron) and v is the value of the carrier velocity expressed in m/s. For example, in the case of electrons (holes) with isotropic effective mass $m_e^* = 0.1 m_o$ ($m_h^* = 0.4 m_o$) and thermal velocity $v_e = 10^5$ m/s, the electron (hole) De Broglie wavelength is equal to $\lambda_{DB,e} \approx 73$ nm ($\lambda_{DB,h} \approx 18$ nm).

In typical semiconductors with electron effective mass $m_e^* = (0.01$–$1)\ m_o$, a De Broglie wavelength of the order of $\sim$730–73 Å (much larger than lattice constant) results at T = 300 K. For decreasing temperatures down to T = 4 K, λ_{DB} increases to 10^2–10^4 Å because of the lower electron thermal velocity. Furthermore, λ_{DB} can depend on the doping conditions due to changes in the carrier density.

In metals, the characteristic length-scale is termed Fermi wavelength (λ_F) and defined as De Broglie wavelength at the Fermi edge E_F (the highest occupied energy level at T = 0 K: any energy state below E_F is occupied and every level above E_F is empty). Based on its definition, the Fermi wavelength is expressed as follows

$$\lambda_F = h/mv_F$$

where $\mathbf{v}_F$ is the electron velocity at the Fermi energy E_F that, in terms of the electron density n at T = 0 K, is given by

$$E_F = (1/2)\, mv_F{}^2 = \left(3\pi^2\right)^{2/3} \left[h^2/\left(2m\right) n^{2/3}\right]$$

For increasing temperature above zero degrees Kelvin some electrons will be excited to higher states thus causing a blue-shift of the energy of the topmost filled level (the chemical potential energy μ) and increasing electron thermal velocity.

For example, in the case of copper (Cu) which is a monovalent element with atomic number Z = 29 and electronic configuration Cu:[Ar] $3d^{10}\ 4\ s^1$, the Fermi velocity is $v_F = 1.57 \times 10^6$ m/s. From the equations $E_F = (1/2)mv_F{}^2$ and $\lambda_F = h/mv_F$, after substituting $m \sim m_o$ [54], it results that $E_F \approx 7$ eV and $\lambda_F \approx 0.46$ nm.

Table 3.1 Fermi energy (E_F), Fermi velocity (v_F), effective mass normalized to the free electron mass (m^*/m_o) and Fermi wavelength (λ_F) of some common metals

Element	E_F (eV)	v_F (10^6 m/s)	m^*/m_o	λ_F (nm)
Li	4.74	1.29	1.28	0.44
Na	3.24	1.07	1.20	0.57
K	2.12	0.86	1.12	0.75
Cu	7	1.57	1.01	0.46
Ag	5.49	1.39	0.99	0.53
Au	5.53	1.4	1.10	0.47
Al	11.7	2.03	1.18	0.30
Zn	9.47	1.83	0.85	0.47

In metals, since the density of the conduction electrons ranges between approximately 10^{28} and 10^{29} electrons/m^3, a Fermi energy of the order of 2–10 eV results that depends on the atomic valency and the electronic density. As Table 3.1 shows, in many common metals, the electron effective mass is close to m_o and $\lambda_F \sim 0.3$–1 nm.

Another characteristic length scale in bulk solids is the average physical separation between the electron and hole, referred to as the "exciton Bohr radius", in a bound electron-hole (e-h) pair (termed "exciton"). The absorption of a photon by an interband transition in a bulk semiconductor or insulator can create an electron in the conduction band and hole in the valence band correlated through the Coulomb interaction. Such a state of an electron and hole bound by the electrostatic interaction is a neutral e-h complex called "exciton" [55–61]. The bulk exciton Bohr radius a_{ex}^{bulk} is given by the following formula

$$a_{ex}^{bulk} = a_H \varepsilon_r (m_o/\mu_r)$$

where $a_H = 0.53$ Å is the Bohr radius of H atom, ε_r is the relative dielectric constant, m_o is the mass of a free electron and μ_r is the reduced mass of the e-h system ($\mu_r = m_e^* m_h^*/(m_e^* + m_h^*)$, being m_e^* and m_h^* the effective masses of the electron and hole, respectively).

Two kinds of excitons can be distinguished, termed Wannier–Mott excitons and Frenkel excitons (Fig. 3.3). The former ones, also called "free excitons", are delocalized (i.e., weak e-h coupling) states with binding energy $\sim$10 meV and mainly occur in semiconductors (large dielectric constant $\varepsilon \sim 10$). The latter ones, also called "tight bound excitons" are characterized by strong e-h coupling with binding energy of $\sim$0.1–1 eV (form in insulator and molecular crystals ($\varepsilon \sim 2$)), localization on specific sites and hopping motion from one site to another. Basically, differences in the binding energies implies that a_{ex}^{bulk} of the Wannier–Mott excitons is larger than a_{ex}^{bulk} associated to Frenkel excitons (Fig. 3.3).

Since in the following we will consider semiconductors, we will deal with Wannier–Mott excitons. The common technological important semiconductors such as Si, Ge, GaAs, GaP, InP, CdSe and InSb, have exciton Bohr radia of 4.9, 17.7, 14, 1.7, 9.5, 3 (5.07), and 69 nm, respectively.
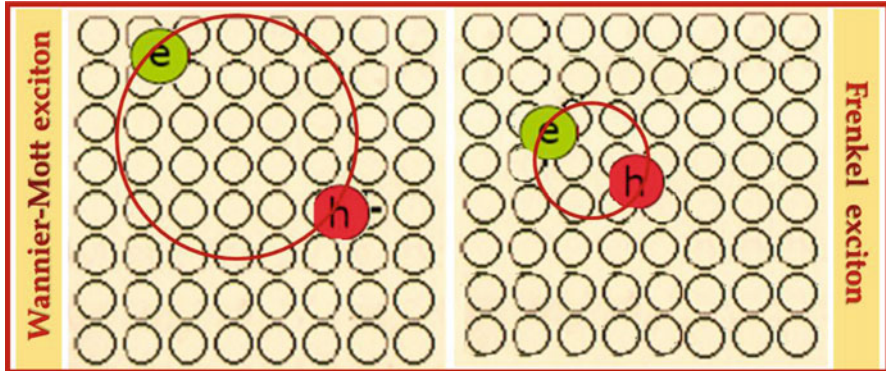
Fig. 3.3 Schematic representation of the two kinds of excitons

Definitively, to summarize, typical solid-state bulk systems can be characterized by their electronic dispersion (band-structure) and the Fermi-Dirac distribution function. Furthermore, characteristic length scales can be defined, namely a De Broglie wavelength of carriers (electrons and holes in semiconductors and electrons in metals) in the picture of the fermion gas and the exciton Bohr radius in semiconductors which is related to e-h pairs coupled by electrostatic interaction.

Once assessed that characteristic length scales exist in solid-state bulk systems and they are of the order of nanometer, it is straightforward to investigate their interplay with the size of the nanostructures in regard to fundamental properties of materials.

3.2.2 Quantum Confinement Effects and Classifications of the Nanostructures

The expression "quantum confinement effects" refers to changes in the electronic band structure and density of states (DOS) resulting from scaling the size of a system down to ultra-small length scales. The meaning of "ultra-small" is critical and can be specified once the interplay between characteristic length scales and size of the system is established. Notably, both optical and electric (transport regimes) properties of materials can be affected by reduction of their size to the nanometer level. On this small length scale electron transport is ruled by quantum mechanics (electron wave behaviour and quantum tunnelling are demanding) and novel phenomena (such as quantized conductance, Coulomb blockade and single electron tunnelling) [62–76] occur which are the subject of "nano-electronics" [77, 78]. Further length scales must be defined to account for the size-dependent electric properties that we will not consider in our discussion focused on the size-dependent

optical properties of nanostructures. In this respect, the regime where the optical properties of semiconductors became size and shape dependent is ruled/set by the bulk exciton Bohr radius a_{ex}^{bulk} or the De Broglie wavelength of carriers in the bulk counterpart. Instead, the Fermi wavelength λ_F is the length-scale associated with confinement effects in metal nanostructures.

The most known and widely studied size-dependent effect is the co-called "quantum-size effect", i.e., the confinement-induced discrete energy spectrum, that occurs whenever a length characteristic (termed "confinement length" hereafter) of the system becomes comparable or smaller than a characteristic length-scale of the bulk counterpart. For example, a semiconductor sample with at least one dimension comparable to or smaller than the De Broglie wavelength of the corresponding bulk material exhibits discrete electron energy along the k-space direction associated to the confinement direction. On the other hand, while in bulk semiconductors, the exciton (Coulomb-bounded e-h complex) can move freely in all directions, an e-h pair forms and feels the system boundaries when a relevant length of a semiconductor is reduced to the same order as the bulk exciton Bohr radius a_{ex}^{bulk} (a few nanometers). In this situation, quantization of the exciton energy spectrum results.

Quantum size effects are also known for metal nanoparticles. However, since the typical De Broglie wavelengths λ_{DB} and exciton Bohr radius a_{ex}^{bulk} in semiconductors are larger than the Fermi wavelength λ_F in metals, then λ_F is the smallest length scale relevant to quantum-size effects and effects of spatial confinement are expected to be more easily observable in semiconductors than in metals. Indeed, being λ_F usually very short in metals (Table 3.1), then localization of the energy levels can be observed in metal nanostructures with size below 2–4 nm, that is whenever the level spacing exceeds the thermal energy ($\sim$25 meV at T = 300 K).

Commonly, nanostructures are classified based on their dimensionality, meaning the number of dimensions (one, two and three) scaled down to the nanometric-length. According to this criterion/standard, mesoscopic structures are termed two-dimensional or briefly 2D (confinement along one direction), one-dimensional or briefly 1D (confinement along two directions) and zero-dimensional or briefly 0D (confinement along three directions). Consistently with this classification, three-dimensional (3D) structure means bulk system. More precisely, the dimensionality of a mesoscopic system refers to the number of degrees of freedom in the particle momentum (Fig. 3.4). Hence, the nomenclature 2D-structure indicates confinement

Fig. 3.4 Classification of the nanostructures based on the number of confinement spatial directions

of the particle motion along one direction (z-direction in Fig. 3.4) and free motion along the other two independent directions (x and y directions in Fig. 3.4).The term 1D-structure means free movement along only one direction (x-direction in Fig. 3.4), i.e., confinement along two directions (y and z directions in Fig. 3.4). Confinement along all the directions defines 0D-structures and the nomenclature 3D structure refers to free motion along any direction. Generally 2D, 1D and 0D systems are also referred to as "quantum well" (QW), "quantum wire" (QWR) and "quantum dot" (QD), respectively. Sometimes 0D nanostructures are termed "quantum boxes" or "artificial atoms" too because electron confinement along all directions implies atom-like electron dispersion, i.e., spectrum consisting of discrete lines accessible to the system at characteristic energies.

In practice, the idea underlying the introduction of nanostructures was to create artificially, by combining different semiconductor materials, potential wells and barriers for confining carriers (electrons and holes) along one, two or three directions. The shape of the confining potential in conduction and valence bands is determined by the offset of band gap between different materials used as well as by the geometry of the structure. Nanostructures are the key systems for band gap engineering purposes in optoelectronics: since the band gap energy of semiconductors determines their emission wavelength, new materials and combination of materials rather than alloys of semiconductors enable to carry out custom-designed emission energies.

3.2.3 Surface to Volume Ratio and Applications

In addition to quantum-size effects, another peculiarity of nanomaterials is the increasing importance of their surfaces with decreasing size that involves chemical and physical properties remarkably different from their macro counterparts. For example, while bulk gold does not react with many chemicals, gold nanoparticles can be used as highly reactive catalysts to speed up reactions due to their size-related reactivity [79–82]. This behavior can be ascribed to the increased surface to volume ratio (SVR) and role played by surface atoms for decreasing size, which is a peculiarity of the nanoworld.

Let there be a cube with sides L and a sphere with radius R (Fig. 3.5). For the cube, the volume and surface area is $V = L^3$ and $S = 6L^2$, respectively. For the sphere, the volume and surface area is $V = (4/3)\pi R^3$ and $S = 4\pi R^2$, respectively. As the characteristic size (L or R) increases, the corresponding increase in the surface area is squared and the increase in the volume is cubed. Hence, surface area and volume decrease for decreasing size with volume increasingly at a much faster rate than the surface area. Instead, since the SVR (S/R) scales with the inverse of the characteristic size (L or R), it increases very fast for decreasing size and the greater the characteristic size, the lower the SVR. In the case of characteristic length of the order of nanometer, a very large SVR would result, meaning that the role and weight of surfaces becomes important in the nanoworld. In fact, increased SVR involves higher contribution of the surface energy to the overall energy, i.e., decreased

Fig. 3.5 Surface to volume ratio (S/V) of a cube and a sphere

$V = L^3$
$S = 6L^2$
$S/V = 6/L$

$V = (4/3)\pi R^3$
$S = 4\pi R^2$
$S/V = 3/R$
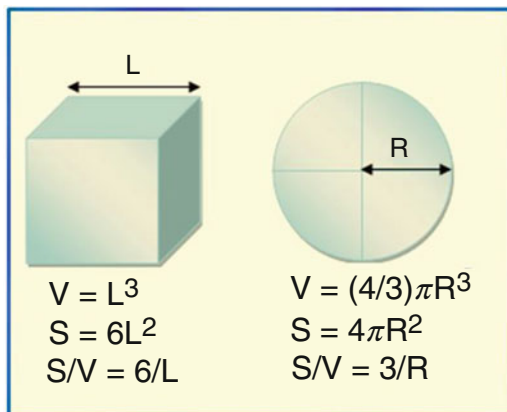
cohesive energy [44, 83]. Moreover, the number of weakly coordinated surface atoms increases with decreasing size [44, 83, 84]. Such increased SVR and number of surface atoms in mesoscopic systems involve important phenomena peculiar of the nanoworld, such as increased surface chemical reactivity and depression of the melting point.

In practice, given a system of nanostructures (for example nanoparticles), the remarkably increased number of surface atoms would favor interactions (chemical reactions and bonds) between the surfaces of contiguous nanostructures as well as between the nanostructures and other chemicals. Therefore, nanoscale sizing maximizes possible reactivity because it maximizes the number of reaction sites. On the other hand, reduced coordination of the surface atoms (i.e., fewer neighboring bonds than inner atoms) reduces the cohesive energy that dominates the thermal stability (melting, evaporation and phase transition) [44, 85]. Since melting stabilizes the total energy by reducing the total surface energy, isolated and substrate-supported metallic, organic and semiconductor low-dimensional systems with relatively free surface fraction melt at temperatures lower than the melting point of the corresponding bulk material [41] and melting can be a surface-initiated process [86–89]. In this respect, the nomenclature "surface melting" or "pre-melting" is used because the mechanism can be modeled as the formation of a disordered "quasi-liquid" layer (where "quasi-liquid" indicates both liquid-like and solid-like) on the surface of an annealed solid system that thickens with increasing temperature and drives the complete melting of the nanostructure [90–92].

Surface melting is also responsible for collapse/breaking up of a continuous film, with thickness ranging from a few nanometers to hundreds of nanometers and deposited on an inert substrate, into patterns that spread, coalesce and decay into discrete droplets under high-temperature heating [93–96].

Such a dewetting phenomenon onsets at temperature lower than the one of bulk melting and is driven by the reduction of surface energy, optimization of shape and reduction of the heat for melting [96]. Therefore, pre-melting, melting and dewetting of low-dimensional systems are stabilizing processes prompted to minimize the

surface energy in the presence of competition between surface and bulk free energy. Also, shape and sharp surface features (surface curvature, stepped surfaces and corners) favor reduced coordination of the surface atoms (i.e., fewer neighboring bonds than inner atoms) and surface diffusion, thus leading to increased surface-energy (reduced cohesive energy) [97–99] and reshaping. In this respect, "edge pre-melting" (i.e., pre-melting appearing at vertices and edges) is the first step of surface melting [100] and involves initial getting rounder and broadly stepped features, due to mostly liquid-like atoms causing increasing mobility of vertex and edge atoms [97, 98, 101]. Another melting phenomenon peculiar of the nanoworld is "superheating", meaning that supported mesoscopic systems can melt below or above the melting point of the corresponding bulk crystal depending on the interface structure and matrix material [102–105]. To predict and explain the depression of the melting point at the nanoscale, a number of theoretical models have been developed, including the Thomson's and Pawlow's models [38, 106–109], the Lindemann criterion [110] and approaches based on the Lindemann melting rule [111–114], phenomenological approaches considering solid–liquid equilibrium (such as the homogeneous melting (HGM) model [38, 41, 115],the liquid skin melting (LSM) model and the liquid nucleation and growth model (LNGM) [111, 115–117], analytical models based on the increase of SVR and reduction of the cohesive energy [118–120], the liquid drop model [83, 121] and the bond-order-length-strength (BOLS) correlation mechanism [83].

Essentially two main classes of approaches can be identified to investigate the thermal stability of nanosystems: thermodynamic approaches, also termed top-down approaches, and bottom-up approaches.

Thermodynamic approaches apply basic concepts of classical thermodynamics (solid-liquid equilibrium, phase change and state variables, Gibb's free energy) to develop equations relating the melting point to the size and shape of a nanoscale-system.

Bottom-up approaches are based on computer modeling (mainly Molecular Dynamic (MD) simulations) and are becoming the mainstream method to investigate the melting behavior of nanoparticles/nanoclusters [91, 122–128]. Even if MD simulations can picture the melting dynamic over time scales of the order of picoseconds (i.e., cannot show the true melting dynamics of a system) and model systems containing a limited numbers of atoms, however they let a more accurate estimation of the melting point and melting processes (pre-melting, edge-melting and influence of shape) at the nanoscale. Indeed, the thermodynamic point of view (that predicts melting at a well-defined (equilibrium) temperature) contrasts with the experimental evidence that shows the lack of a precise melting temperature and, instead, the occurrence of a temperature interval over which melting phenomena can be observed [129, 130]. In the presence of melting point depression, a size-dependent broadening of the range of temperature in which melting occurs can be observed, being the broadening more evident for decreasing particle size.

On the other hand, based on the thermodynamic equilibrium between bulk solid state and bulk liquid state, the change of the melting temperature $\Delta T_m = T_{m,B} - T_{m,NP}$ (where $T_{m,B}$ and $T_{m,NP}$ are the bulk phase and size-dependent

melting point, respectively) can be found to scale linearly as a function of the size R of the nanoparticle (subscript NP). In this calculation isolated, homogeneous and spherical nanoparticles are assumed. Indeed, the experimental findings indicate deviation from a linear trend for small enough (R < 10 nm) size and in the case of supported semiconductor nanoparticles [131–133]. Moreover, shape, substrate and free surface, crystalline orientation and dimensionality must be also considered to realistically model the size-dependent melting process. Therefore, in addition to the difficulty in determining the melting point from experiments, spreading use of MD simulations as compared to thermodynamic approaches is also favored by the conceptual limits of the thermodynamic approach. In this respect, the key question arising from the failing predictions of the conventional thermodynamics applied to the nanoworld is "May classic thermodynamics be applied to model the thermal stability of nanomaterials or, instead, nano-thermodynamics should be developed?"

Even if key issues still need to be understood about the thermal stability of nanomaterials, depression of melting point has important technological applications such as low-temperature (far below the bulk melting temperature) melting of nanostructure distributions resulting in a continuous dense film [130] and large area soldering applications leading to the packaging technology termed "wafer bonding" [134]. Wafer bonding is an emerging technology for fabricating complex three-dimensional structures at temperatures (a few hundreds of Celsius degrees) compatible with the ones required in the processing conditions leading to integration of multi-function microelectronic systems.

Annealing of arrays of nanorods can be used to obtain a dense continuous film going through several temperatures and structure (disordered phase, re-crystallization and formation of larger grains) regimes before the heated nanorods completely melt and collapse into a continuous phase [130, 134]. It is worth noticing that tilt angle change of the nanorods as well as tuning of their diameter and degree of package (reduced gaps between neighboring nanorods) can help their collapse and disappearing (as a result of coalescence) and decrease the annealing temperature requested to carry out a dense continuous film. At the applicative level all of this enables to form a continuous ordered film at much lower temperature as compared to the post-deposition annealing temperature of the counterpart bulk film.

The depression of the melting point can be also exploited to carry out wafer bonding, where two wafers, each consisting of a supported array of nanorods grown by an oblique angle deposition technique, are superposed with the nanorods layer in contact to act as an adhesive upon annealing. This two wafer structure is subsequently subjected to external pressure and heating (even at lower temperature than the collapse temperature of the nanorods) in order to favor first the formation of nano-structured bond at the nanorod/nanorod interface and then eliminate such a bonding interface and structure voids. The resulting sintering of the nanostructures and the formation of a dense bonding layer is not only size-dependent but depends on the bonding pressure too.

Since temperatures as low as a few hundreds Celsius degrees are involved in wafer bonding, this approach is an emerging technology with great promises in advancing integrated 3D chip technology.

3.3   Quantum Mechanical Models in Nanoscience

Low-dimensional systems are excellent examples of quantum mechanics in action
[135]. Quantum confinement effects result essentially from changes in the electronic
dispersion as compared to the bulk counterpart due to the influence of ultra-small
(nanometric) length-scale constraints on the electron wavefunctions. Quantum size
effects occur whenever a characteristic geometric-length of the system becomes
comparable or smaller than a characteristic length-scale of the bulk counterpart.
As a result of such "geometrical" constraints, electrons "feel" the presence of the
structure boundaries and changes in its size as well as shape and adjust their energy
spectrum that becomes discrete. Depending on the material (semiconductor, insula-
tor or metal) and dimensionality of the nanostructure (2D, 1D or 0D nanostructure),
an electronic dispersion with different expression results.

As previously discussed, the bulk characteristic length-scales are the De Broglie
wavelength (λ_{DB}) (termed Fermi wavelength (λ_F) in metals) and the Bohr radius
of an exciton ($a_{ex}{}^{bulk}$) in semiconductors. The basic building-block nanostructures
are QWs (2D dimensional system), QWRs (1D dimensional system) and QDs (0D
dimensional system). In any case, a quantum-mechanical treatment is demanding to
be able to predict the physical behaviour of a low-dimensional structure, meaning
that the Schrödinger equation must be solved in presence of a given quantum-
confinement potential.

In general, in the Schrödinger description of a system the following equation
must be solved

$$\left(-\frac{\hbar^2}{2m^*}\nabla^2 + V(\mathbf{r}, t)\right)\varphi(\mathbf{r}, t) = i\hbar\frac{\partial\varphi(\mathbf{r}, t)}{\partial t}$$

where $\mathbf{r}$ and t are the spatial and temporal coordinates, respectively, $\nabla^2 = \frac{\partial^2}{\partial x^2} +$
$\frac{\partial^2}{\partial y^2} + \frac{\partial^2}{\partial z^2}$ is the Laplacian operator, V($\mathbf{r}$,t) is the potential influencing the system's
motion, m* is the (effective) mass of the system, $\hbar$ is the reduced Planck constant
and $\varphi(\mathbf{r},t)$ is the wave function describing the system. The quantity $|\varphi(\mathbf{r},t)|^2$ is the
probability of finding the system at a spatial location $\mathbf{r} = (x,y,z)$ and time t.

Under the assumption V($\mathbf{r}$,t) = V($\mathbf{r}$) the dependence on time and spatial coordi-
nates can be separated by writing the wave function as a product

$$\varphi(\mathbf{r}, t) = \psi(\mathbf{r})\phi(t) = \psi(\mathbf{r})\exp(-i2\pi Et/h)$$

which leads to the following time-independent Schrödinger equation

$$\left(-\frac{\hbar^2}{2m^*}\nabla^2 + V(\mathbf{r})\right)\psi(\mathbf{r}) = E\psi(\mathbf{r}) \tag{3.1}$$

where E is introduced as a constant to be meant as the energy of the system.

Standard quantum systems in solid state physics are a free (isolated) particle, a particle in a box with either infinite or finite walls and a particle moving under the influence of a periodic potential (such as an electron in a crystal). In all these cases the corresponding time-independent Schrödinger Eq. (3.1) can be solved analytically yielding energy spectrum and electronic wave functions.

A free electron model is the simplest way to interpret the electronic structure of metals. In this approximation the time-independent Schrödinger Eq. (3.1) can be solved for $V(\mathbf{r}) = 0$ and effective mass given by the free electron mass m_o. The resulting solutions have the form of plane-wave functions (i.e., $\psi_k(\mathbf{r}) = A \exp(i\mathbf{k}\cdot\mathbf{r})$, where $\mathbf{k}$ is the wave vector constrained by the periodic boundary conditions) with energies $E = (\hbar k)^2/(2 m_o)$.

Confining a particle along at least one spatial direction introduces quantized energies and wave function changing from a traveling wave to a standing wave [136]. In the most simple case of a particle spatially confined along the x-direction within a distance a (one-dimensional (1D) quantum box of width a) (Fig. 3.6), the effect of the 1D spatial confinement along the x-direction is introduced mathematically by the potential V(x) defined as V(x) = 0 if 0 < x < a (where a is the width of the confining well) and $V(x) = V_o$ elsewhere (where V_o is assumed finite and infinite in the case of a finite and infinite well, respectively) with boundary conditions requiring that the wave functions have nodes at the walls of the potential well. In the case of one-dimensional infinite well the solutions are oscillating functions vanishing at the walls (Fig. 3.6a) and the energy spectrum is discrete with eigenvalues labeled by one quantum number. In the case of a finite well having the same width a, the energies are slightly lower than the corresponding ones of the infinite well and leakage of the wavefunctions into the barrier occurs (quantum tunneling) (Fig. 3.6b) [136], which means that the wave functions are less well confined than in the corresponding infinite well. Notably, there is only a limited number of solutions, but there is always at least one.

Although the infinite-well model is an approximation, it is usually applied as a good starting point for describing the general effects of quantum confinement.

The results of the 1D quantum box can be extended to the two-dimensions (2D quantum box) and three-dimensions (3D quantum box) in a straightforward way. For example, if the particle with mass m is confined to a 2D box in the (x,y) plane of a Cartesian coordinate system, then the well potential V(x,y) is defined as V(x,y) = 0 if 0 < x < a and 0 < y < b (where a and b is the width of the confining well along x and y, respectively) and $V(x,y) = V_o$ elsewhere (where V_o is finite and infinite in the case of finite and infinite well, respectively). The solutions of the time-independent Schrödinger equation are still oscillating functions in each confinement direction and the energy spectrum is discrete with eigenvalues labeled by two quantum numbers, that is

$$E_{n_x,n_y} = \left(\frac{h^2}{8m^*} \right) \left[\left(\frac{n_x}{a} \right)^2 + \left(\frac{n_y}{b} \right)^2 \right]$$
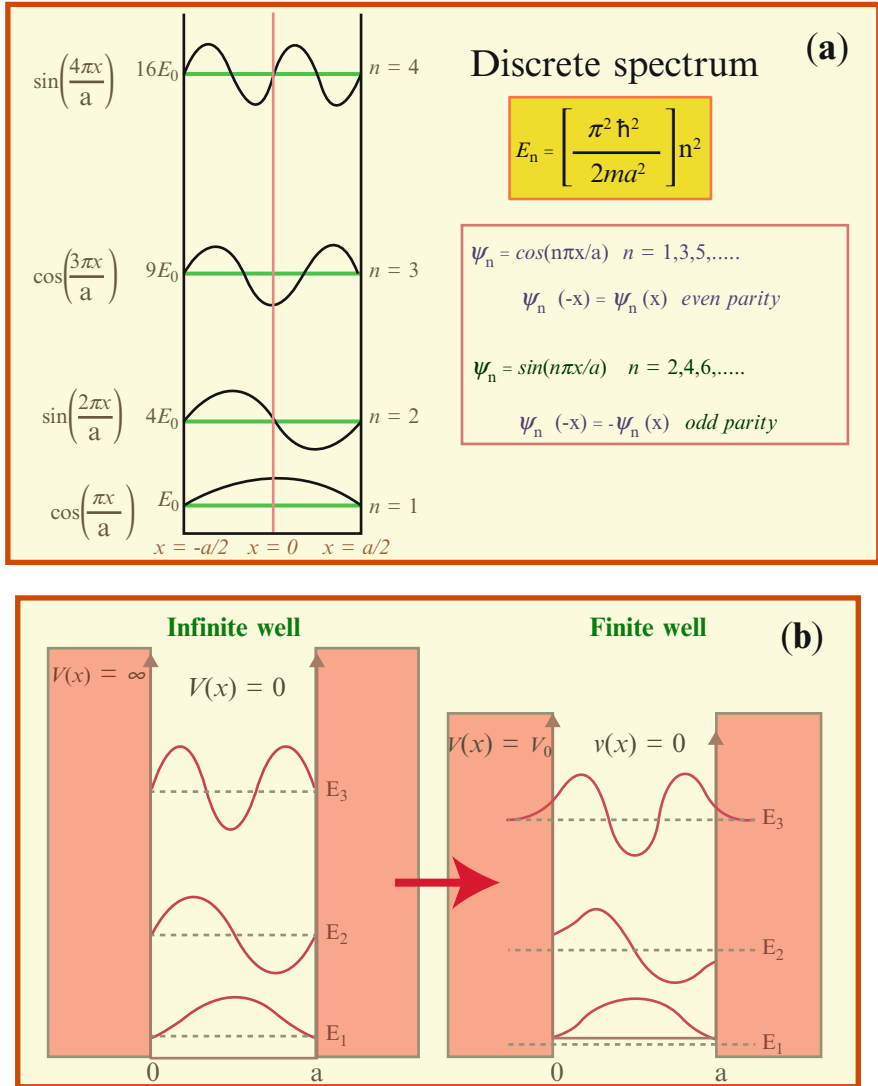
Fig. 3.6 (**a**) Quantized energy spectrum and wave functions of a one-dimensional infinite quantum box of width a. (**b**) Effect of the finite potential barrier versus the infinite one

where n_x and n_y are integers. The energy of the first allowed electron energy level in a typical 100 Å-wide GaAs quantum well is about 40 meV.

The standard problem of a N-dimensional box ($N = 1,2,3$) is the basis of the quantum-mechanical treatment of semiconductor quantum confined structures that, as already outlined, can be classified according to the number of confinement spatial directions. That is, confinement in one, two and three directions defines

2D-structures (termed QWs or quantum films), 1D-structures (termed QWRs) and 0D-structures (termed QDs), respectively. Usually, the theory of nanostructures retains the Bloch description of the bulk properties of a solid-state system but introduces an envelope function to correct for the spatial confinement of the charge carriers (electrons and holes) along one or more directions. In this approximation, the total wave function is expressed as the product of the Bloch function describing the bulk properties of the nanostructure's material and the envelope function that accounts for the spatial confinement effects. The envelope function satisfies a Schrödinger equation for a "particle-in a-box" problem (one-dimensional, two-dimensional and three-dimensional box in the case of a QW, QWR and QD, respectively).

3.3.1 Quantum Confinement in Semiconductor QWs

Quantum wells (QWs) are thin layered semiconductor structures [137, 138] that can be fabricated to a high degree of structural quality and control of thickness by modern epitaxial crystal growth approaches [139]. QWs can be assumed as prototypical systems to discuss the key theoretical concepts relevant to introduce quantum confinement effects and to interpret the electronic and spectroscopic properties of low-dimensional systems.

A semiconductor QW structure results whenever one characteristic geometric length of a semiconductor system is made comparable to or smaller than the electronic De Broglie wavelength λ_{DB} of the corresponding bulk material. In practice a QW is a heterostructure formed through alternating layers of semiconductor materials with different band gaps: the semiconductor (termed A in Fig. 3.7a) with the lowest band gap energy E^A_{gap} (Fig. 3.7b) is sandwiched between two layers of another semiconductor (termed B in Fig. 3.7a) having a larger band gap energy E^B_{gap} (Fig. 3.7b). Therefore, a confining potential well for electrons (holes) in the material A (termed well semiconductor) is introduced by potential barriers involved by the sandwiching layers (material B) (Fig. 3.7b). The well depth for electrons (holes) is the difference (i.e. the offset) between the conduction-band (valence-band) edges of the well and barrier semiconductors. This situation is encountered in practice for the following list of pairs of materials well/barrier: GaAs/GaAlAs, GaAs/GaInP, GaSb/GaAlSb, GaInAsP/InP, GaInAs/AlInAs, InP/GaInAs, Si/SiGe and GaSb/AlSb. In the case of a GaAs/AlGaAs QW, the quantum confinement is provided by the discontinuity in the band gap at the interfaces and the Al concentration is typically around 30 %, leading a band-gap discontinuity of 0.36 eV [140] such that electrons and holes see a confining barrier of 0.24 and 0.12 eV, respectively. The dispersion of a QW can be calculated by solving the Schrödinger equation for the electrons and holes in the potential wells created by the interface band discontinuities. The well width is the thickness of the intermediate layer (termed L_z in Fig. 3.7a, where z is the growth-direction of the tri-layer heterostructure) and represents the length to be made comparable with the bulk de Broglie wavelength of the

Fig. 3.7 A semiconductor QW structure A/B/A: (**a**) alternating layers of semiconductor materials B/A/B with (**b**) the lowest band gap material A sandwiched between two layers of a material B with a larger band-gap in such a way to form a potential well confining the electron motion (**c**) along the growth direction of the heterostructure
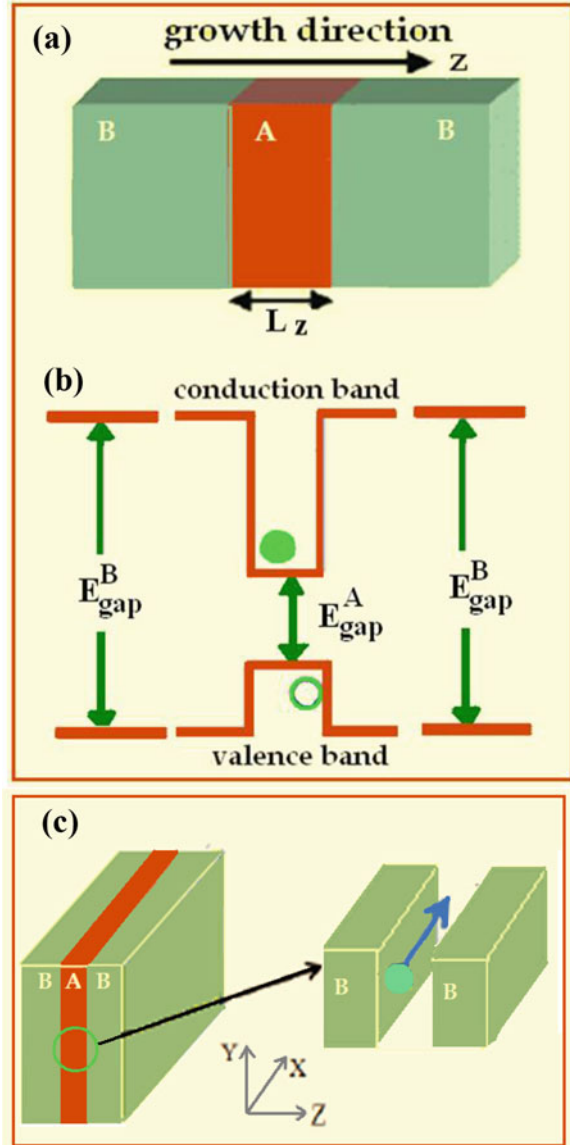
electrons or holes in the material A (λ^A_{DB}) to induce quantum size effects. Materials to be coupled to form a QW should satisfy the further request to be "lattice-matched", that is their lattice constants must be nearly identical, to reduce interface dislocations and defects. In practice relief of strain occurs above a critical thickness. Indeed, QWs can be routinely grown as strained layers on top of a lattice with a different cell constant (e.g., $In_xGa_{1-x}N/GaN$, $In_xGa_{1-x}As/GaAs$, and $Si_{1-x}Ge_x/Si$ QWs) as long as the total thickness of the strained layer is less than a critical value

above which interface misfit dislocations form. For example, a defect-free strained In_xGa_{1-x} As/GaAs QW can be grown with x = 0.2 and L_z of nearly 10 nm.

The well width is the thickness of the intermediate layer (termed L_z in Fig. 3.7a, where z is the growth-direction of the tri-layer heterostructure) and is the characteristic geometric length to be compared with λ^A_{DB} to observe quantum-size effects [140, 141]. In GaAs, where the electron effective mass amounts to 0.067 m_0, the De Broglie wavelength $\lambda_{DB} = 42$ nm at 300 K results, meaning structures of thickness ≈ 10 nm are needed in order to be able to induce quantum-confinement effects at room temperature. If the thickness of the well material is comparable to or smaller than the De Broglie wavelength of the corresponding bulk material, based on the simple "particle in a 1D box" model, the motion of carriers is expected to be confined in the direction perpendicular to the layers (growth-direction) and free in the QW plane (Fig. 3.7c). In order to demonstrate that the allowed states in a QW correspond to standing waves in the direction perpendicular to the layers (growth-direction) and plane waves in the QW plane, the time-independent Schrödinger Eq. (3.1) must be solved in the simple "particle in a 1D box" approximation (of the envelope function) [142–145] where the well potential is the QW potential (Fig. 3.8a, b).
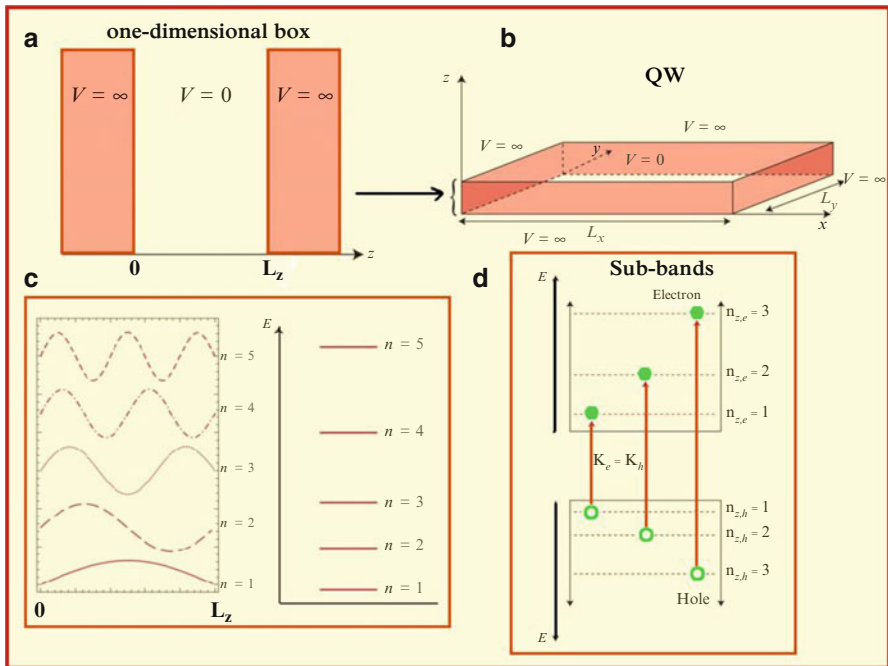

Fig. 3.8 Schematic diagram of (**a**) the potential barrier, (**b**) layer structure, (**c**) quantized eigenfunctions and eigenvalues and (**d**) band diagram with subband-structure (*dashed lines*) of a QW of thickness Lz and infinite barrier wall

Accounting for the structure geometry and presence of materials A and B (Fig. 3.7a), the QW potential can be written as follows:

$$V_{QW}(x, y, z) = V_A(x, y, z) \, F_A(z) + V_B(x, y, z) \, F_B(z)$$

where the functions $F_A(z)$ and $F_B(z)$ introduce the potential of the corresponding layer, that is $F_A(z)$ vanishes in the layer B and $F_B(z)$ vanishes in the layer A in such a way that $V_{QW}(x,y,z) = V_A(x,y,z)$ in the layer A and $V_{QW}(x,y,z) = V_B(x,y,z)$ in the layer B. Since the QW geometry decouples (x,y)-plane and z-direction, the QW potential can be decomposed as

$$V_{QW}(x, y, z) = V^{xy}{}_{QW}(x, y) + V_{QW}(z)$$

where $V_{QW}(z) = V^A F_A(z) + V^B F_B(z)$ is the confining potential seen by the carrier (electron and hole) along the direction z.

On the other hand, the translational invariance of the QW system in the (x,y)-plane enables to model the wavefunctions describing the motion in the QW plane as plane waves. Hence, being m* the carrier effective mass, a general solution of the time-independent Schrödinger equation associated with $V^{xy}{}_{QW}(x,y)$ and motion in the (x,y)-plane can be written as follows:

$$\varphi\left(\mathbf{r_{xy}}, z\right) = \frac{1}{\sqrt{S}} \left(e^{i\mathbf{k_{xy}} \cdot \mathbf{r_{xy}}}\right) \psi(z)$$

where z is the confinement direction (growth-direction), $\mathbf{r_{xy}} = (x, y)$ and $\mathbf{k_{xy}} = (k_x, k_y)$ is the position vector and wave vector in the QW-plane ((x,y)-plane), respectively, and the prefactor is a normalization constant. Therefore, being m* the carrier effective mass, the Schrödinger's equation to be solved for the particle of interest (electron or hole) in a QW is the following one-dimensional time-independent Schrödinger equation:

$$\left(-\frac{\hbar^2}{2m^*}\frac{\partial^2}{z^2} + V_{QW}(z)\right)\psi_n(z) = E_n\psi_n(z)$$

where $\psi_n(z)$ and E_n are the energy eigenfunction and eigenvalue (confinement energy) associated with the n-th solution and it is assumed that $L_z \leq \lambda^A{}_{DB} \ll L_x, L_y$. Rather than the continuity condition of the derivative of the wave functions at the interfaces, the conservation of both wave function $\psi_n(z)$ and particle flux $((1/m^*)(\partial\psi_n(z)/\partial z))$ across the QW walls is the boundary condition to be imposed to match the solutions in the well and the barrier materials. Essentially the equation to be solved is the time-independent Schrödinger equation of the standard problem of a particle confined in a one-dime1D box whose solutions are known to be standing waves (Fig. 3.6) labeled by one integer number.

In the case of an infinitely deep QW heterostructure, the solutions $\psi_n(z)$ of the time-independent Schrödinger equation are analytically known (oscillating sin and

cos functions with nodes at the walls) and the energy spectrum is discrete (Fig. 3.8c) with eigenvalues

$$E_{n_z} = \left(-\frac{\hbar^2}{2m^*}\right)\left(\frac{n_z\pi}{L_z}\right)^2 \text{ where } n_z = 1, 2, 3, \ldots$$

Given the eigenvalue corresponding to $n_z = 1$

$$E_1 = \left(-\frac{\hbar^2}{2m^*}\right)\left(\frac{\pi}{L_z}\right)^2$$

the energy spectrum can be expressed as

$$E_n = E_1 n_z^{\,2} \text{ where } n_z = 1, 2, 3, \ldots$$

Notably, the confinement energies E_{nz} are referred to the bottom of the well and the non vanishing energy E_1 is located above the bottom of the well.

Spacing between subsequent eigenvalues can be easily expressed as

$$E_{n_z+1} - E_{n_z} = \left(\frac{\hbar^2}{2m^*}\right)\left(\frac{\pi}{L_z}\right)^2 (2n_z + 1) \text{ where } n_z = 1, 2, 3, \ldots$$

Therefore, the QW confinement energies are quadratically spaced and their energy spacing increases for decreasing well width L_z and effective mass m^* as well as for increasing quantum number n_z.

The solution of the QW problem for finite well height must be performed numerically and yields bound states whose wave functions are again standing oscillating functions inside the quantum well and exponentially decaying into the barriers (Fig. 3.6) with eigen-energies always somewhat lower than those of the infinite case [146]. In any case, the solution of the QW problem leads to discrete sequences of valence and conduction energy levels (termed sub-bands) (Fig. 3.8d). As the reduced translational symmetry of a QW structure lifts the bulk degeneracy of the heavy-hole (hh) and light-hole (lh) valence bands, each valence sub-band in Fig. 3.8d is a doublet of hh and lh subbands with the hh subband closer to the valence band bottom than the corresponding lh subband. Therefore, hh-to-conduction edge starts at a slightly lower energy and is more closely spaced than the lh-to-conduction edge.

Definitively, if $L_z \leq \lambda^A_{DB} \ll L_x, L_y$ and the effective mass is assumed isotropic, the total energy of a carrier in a QW is given by the formula

$$E_{nz}^{tot} = E_x + E_y + E_{nz} = \left(\frac{\hbar^2 k_x^{\,2}}{2m^*}\right) + \left(\frac{\hbar^2 k_y^{\,2}}{2m^*}\right) + \left(\frac{\hbar^2}{2m^*}\right)\left(\frac{n_z\pi}{L_z}\right)^2$$

$$\text{where } n_z = 1, 2, 3, \ldots$$

where the eigenvalues E_x and E_y are associated to plane waves solutions describing the free motion of a carrier along the x and y directions, respectively, and E_{nz} are the bounded energies of the carrier labeled by the integer index n_z. Since the confinement energies are inversely proportional to both the well width L_z and the carrier effective mass, narrow wells as well as lighter particles involve larger confinement energies. In a typical GaAs/Al$_{0.3}$Ga$_{0.7}$As QW with $L_z = 10$ nm, the confinement energy for electrons and holes is 245 meV and 125 meV, respectively. The infinite well model predicts lowest quantized energies of $E_1 = 30$ meV and $E_2 = 113$ meV for the electrons [147, 148] and 11 meV (40 meV) and 44 meV (160 meV) for the first two bound states of the heavy (light) holes. Notably, the energy spacing of the electron levels should be larger than $k_B T$ at 300 K (i.e., 25 meV) to make the quantum size effect readily observable at room temperature.

The above considerations result in the typical band structure depicted in Fig. 3.9: since the electronic dispersion is parabolic along the direction of free motion, the occurrence of discrete spectrum along the confinement direction (growth direction of the QW) implies a discrete sequence of parabolic bands ("sub-bands") with minimum energy given by the discrete confinement energy along z ($E_x = E_y = 0$). Basically, in a QW carriers (electrons and holes) are free to move in any direction parallel to the QW layers and a carrier in a given confined state can have additionally any amount of kinetic energy corresponding to its in-plane free motion that implies any energy greater than or equal to the confined- energy of that sub-band.
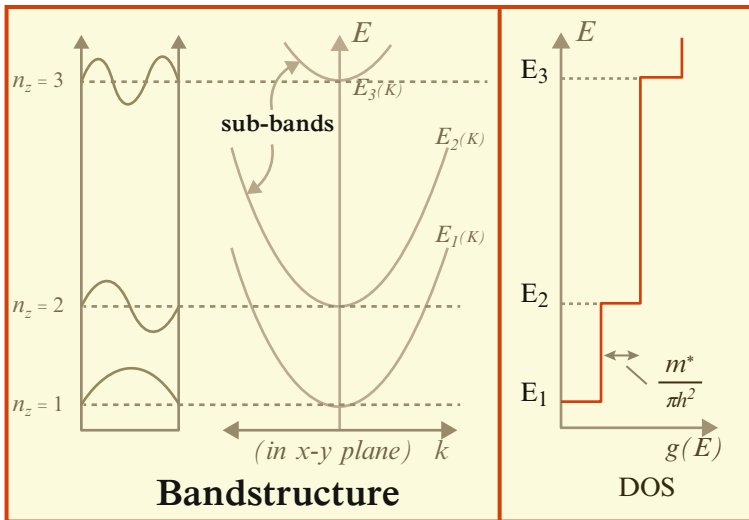

Fig. 3.9 Electronic dispertion of a QW: In a QW, as a result of the carrier confinement along the growth direction and its free motion in the QW plane, the electronic dispertion consists of parabolic subbands leading to a step-like DOS

The subband-structure that characterizes the energy spectrum of a QW determines its spectroscopic properties [149]. The optical transitions in QWs are termed "inter-subband transitions" and take place between electronic states that are confined in the z-direction and free in the well x–y plane.

In a bulk semiconductor, an optical transition is allowed between states having the same k-values in the case of a direct-gap material and momentum is conserved via a phonon interaction in the case of an indirect bandgap material. Turning to a QW, allowed interband transitions can occur according to the following relationship between exciting photon energy ($\hbar\omega$), energy gap of the bulk counterpart of the well material (E_g), energies of the valence (E_{nz}) and conduction (E_{mz}) subbands measured from the valence and conduction edges of the bulk material, respectively:

$$\hbar\omega = E_g + E_{nz} + E_{mz} = E_g + \left(\frac{\hbar^2\pi^2}{2m_h^* L_z^2} \right) n_z^2 + \left(\frac{\hbar^2\pi^2}{2m_e^* L_z^2} \right) m_z^2$$

under the selection rule that only transitions between states of the same quantum number in the valence and conduction bands are allowed. Indeed, in a QW, optical transitions must still conserve momentum in the plane of the QW, just as for bulk semiconductors. Instead of momentum conservation, there is an additional selection rule for the direction perpendicular to the layers resulting from optical absorption strength proportional to the overlap integral of the conduction and valence (envelope) wave functions. The transition rate is proportional to both the square of the overlap of the envelope wave functions and the joint density of states [150]. In the case of an infinitely deep well, the wave functions are orthogonal unless $n_z = m_z$, which gives a selection rule of the quantum number. Transitions between states of different parity are strictly forbidden.

For transitions among the lowest energy states ($m_z = n_z = 1$), meaning the fundamental absorption, the energy band gap of the QW can be calculated, that is:

$$\hbar\omega = E_g^{QW} = E_g + \left(\frac{\hbar^2\pi^2}{2L_z^2} \right) \left(\frac{1}{m_h^*} + \frac{1}{m_e^*} \right)$$

Being in any case $\hbar\omega > E_g$, a blue-shift by the sum of the electron and hole confinement energies of the fundamental absorption as compared to the bulk energy gap E_g is characteristic of a quantum-confined QW heterostructure. Moreover, such a blue-shift may be tuned by adjusting the well width L_z and the well material (i.e., the effective masses of electron (m_e^*) and hole (m_h^*)). Therefore, a practical advantage of confined structures over bulk materials is a wider and tunable band gap energy.

In general, the knowledge of the electronic dispersion lets calculate the density of states (DOS), i.e., the number of allowed energy states per unit volume and unit energy interval, based on the formula

$$g(E) \equiv \sum_n \int_{BZ} d\vec{k}\, \delta\left(E - E_n\left(\vec{k} \right) \right)$$

where E is a given allowed energy, g(E) dE is the total number of electronic states with energy ranging from E to E + dE per unit volume, the sum is extended to all the allowed values of the discrete band-index n, the integral sums all the wave vectors and averages on all allowed spin states.

If the band structure of a QW consisting of parabolic subbands is considered, then the corresponding DOS (per unit energy, per unit surface area) is given by the following expression

$$g^{QW}(E) = \frac{m^*}{\pi\hbar^2} \sum_{n_z} \theta(E - E_{nz})$$

where n_z is the quantum number associated with the confinement energy along the z-direction, $\theta(E-E_{nz})$ is the Heaviside unit step function defined by $\theta(E-E_{nz}) = 0$ if $E < E_{nz}$ and $\theta(E-E_{nz}) = 1$ if $E > E_{nz}$ and a factor 2 for spin has been included. Therefore, it results:

$$g^{QW}(E) = 0 \qquad \text{if } E < E_1$$

$$g^{QW}(E) = \frac{m^*}{\pi\hbar^2} \quad \text{if } E_1 < E < E_2$$

$$g^{QW}(E) = \frac{2m^*}{\pi\hbar^2} \quad \text{if } E_2 < E < E_3$$

Therefore, DOS associated to a QW for a given subband is a "step-like" function starting at the appropriate confinement energy [151]. Since in QWs, just as for bulk semiconductors, absorption transitions follow the DOS profile, the absorption coefficient (i.e., the change in the intensity of the photon flux per unit length) of a QW is a series of steps each corresponding to a QW subband [152].

To summarize, quantizing the carrier motion along the z-direction has three main consequences; (i) a blue-shift of the bulk band edge depending on QW's material and width, which enables effective band-gap engineering; (ii) an increase of the radiative recombination probability by keeping electrons and holes closer together due to the spatial confinement; and (iii) a DOS independent on energy (step-like profile) in contrast to that of the bulk counterpart.

The above approach (free-electron gas approximation) deals with absorption processes in which an exciting photon creates a free electron-hole pair without considering the effect of electron-electron correlation. The considered independent-electron approximation leads to an energy spectrum of carriers independent on the presence of other similar carriers which is taken into account only by populating the allowed energy states according the Pauli's exclusion principle. However, the electron-electron (electron-hole) interactions are important to a more accurate description of physical phenomena such as optical absorption below away from the band-edges. The influence of electron-electron correlation is addressed by excitonic effects in semiconductors that are introduced by defining the exciton as an electron-hole pair bounded by Coulomb interaction. As already discussed, the Wannier excitons, that are classified as weakly bounded excitons, form in semiconductor

materials. Their large size makes them strongly sensitive to nanometer-scale variations of the surrounding, meaning to spatial confinement in nanostructures.

In bulk semiconductors the spectroscopy of (Wannier) excitons can be calculated based on the Schrödinger Eq. (3.1) solved within the approximation that treats electron and hole as two particles moving with the effective masses of the conduction ($m_e{}^*$) and valence ($m_h{}^*$) bands, respectively, and attracted to each other by the Coulomb interaction (according to a modified Bohr model of the hydrogen atom):

$$\left(-\frac{\hbar^2}{2m_e^*}\nabla_e{}^2 - \frac{\hbar^2}{2m_h^*}\nabla_h{}^2 - \frac{e^2}{4\pi \in |\mathbf{r_e} - \mathbf{r_h}|} \right) \varphi_{exc}(\mathbf{r_e},\ \mathbf{r_h}) = E_{exc}\varphi_{exc}(\mathbf{r_e},\ \mathbf{r_h})$$

Upon the transformation of coordinates defined by $\mathbf{r} = \mathbf{r_e} - \mathbf{r_h}$ and the $\mathbf{R_{CM}} = (m_e{}^*\mathbf{r_e} + m_h{}^*\mathbf{r_h})/(m_e{}^* + m_h{}^*)$, the above two-body Schrödinger equation can be separated into an equation for the wave function $F(\mathbf{r})$ of the relative motion of the electron-hole system and an equation describing the motion of the center of mass (CM) by the wave function $G(\mathbf{R_{CM}})$:

$$\left(\frac{\hbar^2}{2m_r^*}k^2 - \frac{e^2}{4\pi \in |\mathbf{r}|} \right) F(\mathbf{r}) = E_r F(\mathbf{r})$$

$$\left(\frac{\hbar^2}{2(m_e^* + m_h^*)}K^2 \right) G(\mathbf{R_{CM}}) = E_{CM}G(\mathbf{R_{CM}})$$

where $1/m^*{}_r = (1/m^*{}_e + 1/m^*{}_h)$ is the reduced mass of the electron-hole system, $\mathbf{K} = \mathbf{k_e}\text{-}\mathbf{k_h}$ is the wave vector of the CM motion and $\mathbf{k} = (m_e{}^*\mathbf{k_e} + m_h{}^*\mathbf{k_h})/(m_e{}^* + m_h{}^*)$ is the wave vector of the relative motion.

Since the Coulomb interaction depends on the relative coordinate, as a result, the CM motion can be pictured as a free motion (plane wave solution) of a particle with total mass $M = m^*{}_e + m^*{}_h$ and the equation of the relative motion is mathematically the Schrödinger equation of the hydrogen atom. Therefore the dispersion relationship of the exciton can be written as follows

$$E_{n,K\ ex} = E_g + E_{CM} + E_r = E_g + \frac{\hbar^2}{2M}K^2 - \frac{R_y^*}{n^2}$$

where E_g is the band gap energy of the bulk semiconductor (i.e., the energy without the Coulomb interaction), E_{CM} is the CM energy (kinetic energy of the exciton) given by

$$E_{CM} = \frac{\hbar^2}{2M}K^2$$

E_r is the discrete spectrum energy of the electron-hole bound states labeled by a principal quantum number $n = 1,2,3,\ldots$ and expressed as follows

$$E_r = -\frac{R_y^*}{n^2}$$

and $R_y{}^*$ is the exciton Rydberg given by

$$R_y^* = \left(\frac{m_r^*}{m_o\epsilon_r^2}\right) R_y$$

where ε_r is the relative dielectric constant of the semiconductor, m_o is the mass of the free electron and $R_y = 13.6$ eV is the atomic Rydberg constant. Therefore, the spectrum of the relative motion of an exciton is a Rydberg series similar to that of the hydrogen atom with an effective Rydberg constant modified by the reduced mass of the exciton and the dielectric relative constant of the material.

The exciton (envelope) functions solving the Schrödinger equation of the relative motion are the known hydrogen-like functions with the ground state solution given by

$$F(r) = F_{100}(r) = \frac{1}{\sqrt{\pi a_{ex}^3}} e^{-r/a_{ex}^{bulk}}$$

where

$$a_{ex}^{bulk} = a_H \varepsilon_r \frac{m_o}{m_r^*}$$

is termed "Bohr radius of exciton" and $a_H = 0.53$ Å is the Bohr radius of the hydrogen atom. In the case of Si, Ge and GaAs, $a_{ex}{}^{bulk}$ amounts to 4.3, 11.5 and 12.4 nm, respectively. Physically, $a_{ex}{}^{bulk}$ is the relative electron-hole separation in the pair coupled by the Coulomb interaction (exciton) and, as already mentioned, represents a characteristic confinement length-scale in semiconductors.

As compared to the independent-electron approximation (leading to the bandstructure in Fig. 3.10a and the absorption coefficient in Fig. 3.10b), accounting for the electron-hole Coulomb correlation (i.e., excitonic effects) leads to a modified bandstructure that describes the system in terms of the electron-hole momentum and consisting of a sequence of discrete bands lying below the conduction band of the continuum of electronic states of the one-electron model (Fig. 3.11a). Such discrete excitonic bands approach the band-edge becoming closer and closer for increasing exciton energy.
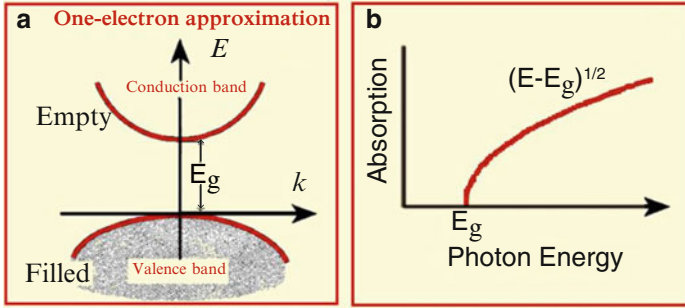
Fig. 3.10 Typical (**a**) bandstructure and (**b**) absorption coefficient of a bulk semiconductor in the framework of the independent-electron approximation
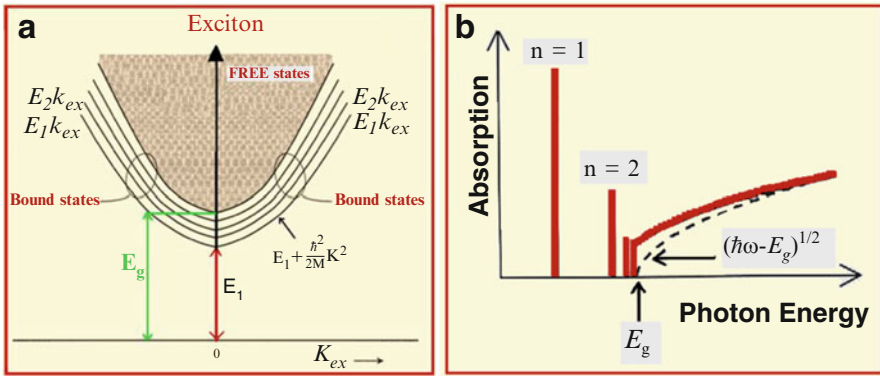

Fig. 3.11 Typical bulk semiconductor (**a**) bandstructure including excitonic contribution and (**b**) absorption coefficient with (*solid line*) and without (*dashed line*) excitonic effects

As for the spectroscopy in the presence of excitonic effects [138], while unbound electron-hole pairs can be continuously generated by interband absorption of photons with energy at least equal to the fundamental band-gap (E_g), for photon energy decreasing below E_g excitons can be created at discrete energies leading to sharp absorption peaks (Fig. 3.11b). Figure 3.11b sketches the main features of the absorption coefficient in the presence (solid line) and in absence (dashed line) of excitonic effects. It can be observed that as the exciting photon energy becomes lower than E_g, the (unbound electron-hole pairs) continuum absorption curve of a direct gap semiconductor with excitonic effects included doesn't decrease to zero according to the square-root trend of the one-electron model (Fig. 3.10b). Instead the absorption coefficient remains finite at the band edge and exhibits strong absorption peaks associated with the ground state (n = 1) and the first excited state (n = 2) of the exciton just below E_g (Fig. 3.11b). Basically, near the band edge, the absorption

coefficient in the presence of excitonic effects (α_{ex}) can be related to the absorption coefficient without excitonic effects (α) as follows

$$\alpha_{ex} = \alpha \left(\frac{2\pi \sqrt{R_y^*}}{(\hbar\omega - E_g)^{1/2}} \right)$$

Finite enhanced absorption below E_g stemming from exciton formation is expressed by the Sommerfeld enhancement factor (i.e., the Coulomb-enhanced absorption coefficient divided by the absorption without Coulomb effects). In practice, in bulk semiconductors excitonic effects can be observed only in optical spectra at very low temperature in truly pure samples because of the low binding energy R_y^* [153]. Indeed, in technologically important bulk semiconductors, such as Si, Ge, and GaAs, the exciton binding energy R_y^* ranges from 3.8 to 14.7 eV, meaning it is lower than the thermal energy ($k_B T = 25$ meV at room temperature). As a consequence, excitonic resonances are not observed because exciton usually dissociates easily at room temperature and merging of excitonic resonances with interband transitions is also favored in poorer quality bulk samples.

Instead, the spatial confinement of carriers in QWs greatly enhances the binding energy of excitons and the oscillator strength in such a way that excitonic effects become observable at room temperature in the optical spectra of QWs as sharp resonances. Basically, exciton binding energy is related to the probability to have electron and hole in the same unit cell which is expressed by an overlap integral of the electron and hole wave functions in the QW. Spatial confinement is expected to strength the electron-hole interaction, thus enhancing the exciton binding energy through an increased overlap integral, and a decreased ground state electron-hole distance (Bohr radius of exciton) of the QW exciton (Fig. 3.12).
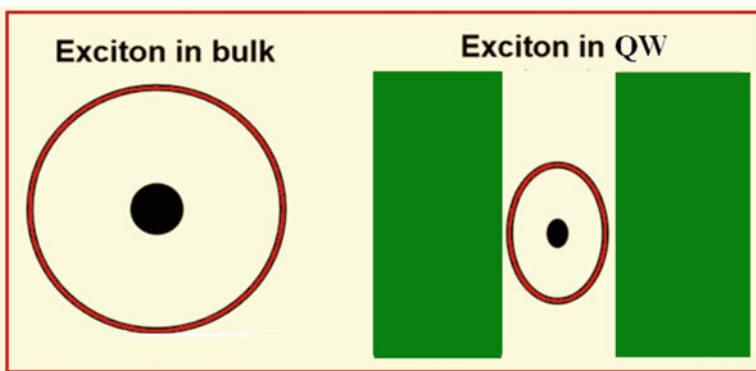

Fig. 3.12 Cartoon of the effects of the spatial confinement on an exciton in a QW: strengthed electron-hole interaction and decreased ground state electron-hole distance (excitonic Bohr radius)

To address the exciton problem in a QW, a time-independent Schrödinger equation must be solved with potential given by the sum of the QW confinement potentials of electron and hole ($V_e(z_e)$ and $V_h(z_h)$, respectively, being z-axis the growth direction of the QW structure) in the one-particle picture and the electron-hole Coulomb interaction:

$$\left(-\frac{\hbar^2}{2m_e^*}\nabla_e{}^2 - \frac{\hbar^2}{2m_h^*}\nabla_h{}^2 + V_e\left(Z_e\right) + V_h\left(Z_h\right) - \frac{e^2}{4\pi \in |\mathbf{r_e}-\mathbf{r_h}|} \right) \varphi_{exc}\left(\mathbf{r_e},\ \mathbf{r_h}\right)$$

$$= E_{exc}\varphi_{exc}\left(\mathbf{r_e},\ \mathbf{r_h}\right).$$

In general, such a problem doesn't have simple analytic solution because the parabolic approximation can be poor for holes, a QW system is a quasi 2D system and the effect of the well size and finite well depth must be considered [154, 155]. Under the assumption that the QW width is less or comparable to the bulk exciton Bohr diameter, then electron and hole are quantized independently of each other and a variational approach can be considered that introduces a class of trial functions with the following form

$$\varphi_{ex} = F\left(R\right)\ f\left(\rho\right)\ U_e\left(z_e\right)\ U_h\left(z_h\right)$$

where R is the exciton center of mass coordinate, ρ is the radius-vector of electron and hole relative motion in the QW-plane, F(R) describes the exciton center of mass motion, $f(\rho)$ describes the relative electron-hole motion in the plane of the QW, $U_e(z_e)$ and $U_h(z_h)$ describe the electron and hole confined motion, respectively, and the following normalization is assumed:

$$\int dz_e |U_e\left(z_e\right)|^2 = \int dz_h |U_h\left(z_h\right)|^2 = \int_0^\infty 2\pi\rho d\rho |f\left(\rho\right)|^2 = \int_0^\infty 2\pi RdR |F\left(R\right)|^2 = 1.$$

In the ideal 2D case, $|U_{e,h}\left(z_{e,h}\right)|^2 = \delta(z_{e,h})$ under the parabolic assumption for carriers, the equation for $f(\rho)$ is the exactly solvable one of a 2D hydrogen atom problem. Therefore, the energy spectrum is given by

$$E_{ex}^{QW} = E_g + E_{nz,e} + E_{mz,h} - \frac{R_y^*}{\left(n-\frac{1}{2}\right)^2} + \frac{\hbar^2}{2M}\left(K_x^2 + K_y^2\right)$$

where $E_{nz,e}$ and $E_{mz,h}$ refer to subband energies of electron and hole, respectively, resulting from the one-particle approximation (Fig. 3.8d), n = 1,2,3 . . . is an integer and $K^2 = K_x{}^2 + K_y{}^2$ [156]. Therefore, including the excitonic effects implies that the eigen energies of the QW calculated in the single particle approximation (i.e., $E_g + E_{nz,e} + E_{mz,h}$) are shifted by the Rydberg energy $\left(-\frac{R_y^*}{\left(n-\frac{1}{2}\right)^2} \right)$ plus the kinetic

energy $\left(\frac{\hbar^2}{2M}\left(K_x^2 + K_y^2\right)\right)$ of the exciton in the QW. As a general trend, while in bulk, the total energy of the exciton is simply the energy of the bang gap plus the exciton binding energy, in a nanostructure there are additional components due to the electron and hole confinement energies

By setting n = 1 (ground state), it can be observed

$$E_{bind,exc}^{QW} = 4R_y^* = 4\,E_{bind,exc}^{bulk}$$

that is, the binding energy of the exciton in an infinite QW is four times the binding energy of the corresponding bulk exciton. This fact lets observe excitonic effects at room temperature in QWs, in contrast to bulk semiconductors where they are only usually observed at low temperatures. Furthermore, in a QW, the electron-hole separation (Bohr radius of the exciton) decreases with respect to the bulk counterpart (Fig. 3.12). This is consistent with increasing binding energy in low-dimensional systems. In the 2D case,

$$E_{bind,exc}^{QW} = 4R_y^* = 4\,E_{bind,exc}^{bulk}$$

$$a_{exc}^{QW} = \frac{1}{2}\,a_{exc}^{bulk}$$

In the case of a realistic QW, a more complex expression of the exciton binding energy is obtained by the variational approach that, after minimization with respect to a variational parameter, yields that the exciton binding energy in a QW ranges from $E_{bind,exc}^{bulk}$ to $E_{bind,exc}^{QW}$. Moreover, it depends on the QW width and barrier heights for electrons and holes and increases for increasing exciton confinement: while for wide QWs the confinement increases for decreasing QW width, for very narrow QWs the opposite occurs due to leakage of the carrier wave function into the barriers.

In regard to excitons in QWs, they are characterized by two regimes depending on the relationship between the well thickness L_z and the bulk Bohr radius of the exciton a_{ex}^{bulk}: strong confinement if $L_z \sim a_{ex}^{bulk}$ and weak confinement if $L_z \gg a_{ex}^{bulk}$. Strong confinement regime (also termed "quasi-2D regime") means that the exciton binding energy is smaller than the confinement energy of the carriers (electrons and holes) and the exciton binding energy as well as the oscillator strength enhance on reducing the well thickness L_z. Weak-confinement regime (also termed "3D regime") means that the exciton binding energy is larger than the carrier quantization energy and the center-of-mass motion of the exciton is quantized as a whole and the oscillator strength is proportional to L_z [157].

The enhanced binding energy and increased oscillator strength of a exciton confined in a QW have critical impact on the spectroscopic properties, that can become dominated by the excitonic effects even at room temperature [154, 155, 158–162]. In this regard, Fig. 3.13c sketches the theoretical absorption spectrum
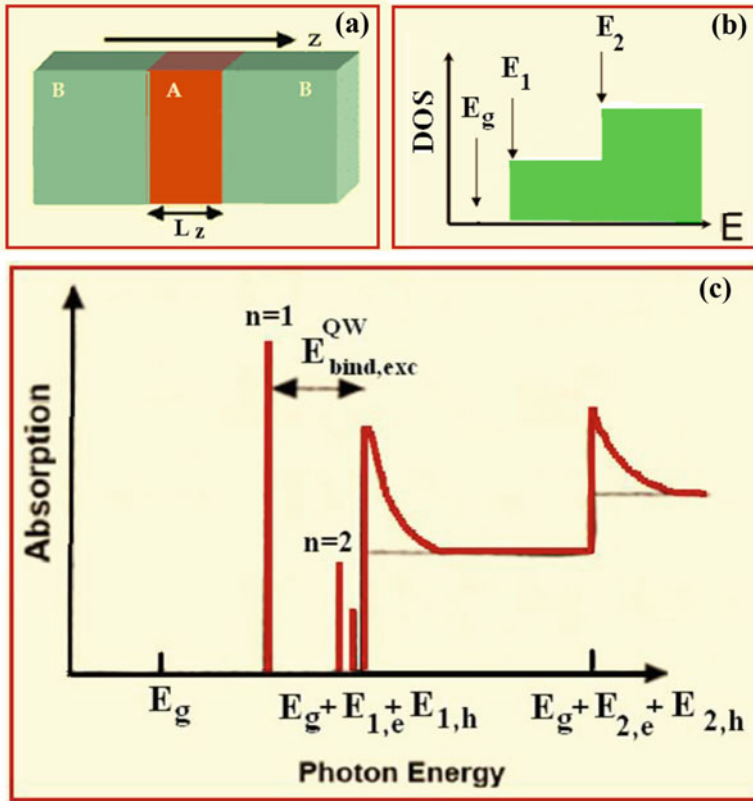
Fig. 3.13 (**a**) QW heterostructure and (**b**) its step-like DOS. (**c**) Sketched theoretical characteristic step-like absorption spectrum of a QW including excitonic effects (sharp intense absorption peaks just below the band-gap energy of the QW)

of a QW including excitonic effects: sharp intense absorption peaks just below the band-gap energy of the QW are associated to the exciton discrete spectrum and the characteristic step-like absorption stemming from the step-like profile of the DOS (Fig. 3.13b) results modified near the absorption edge, as observed in bulk materials while including excitonic influence (Fig. 3.11). The absorption profile of the QW above the exciton lines reflects the constant DOS in 2D, which differs from the increasing absorption of the bulk material resulting from the parabolic 3D DOS.

Indeed, the continuum absorption coefficient is increased over the value without excitonic effects (grey curve in Fig. 3.13c) by the Sommerfeld factor which expresses the influence of the electron-hole correlation on the unbound states. Excitonic features and their appearance can also be modulated by the well thickness

(L_z) [153]. Separate transitions are usually observed for the hhs anf lhs, as a consequence of their different effective masses and lower symmetry of the QW as compared to the bulk counterpart material.

3.3.2 Quantum Confinement in Semiconductor QWRs

Since the study by Esaki and Tsu [137] in the 1970s about semiconductor QWs and superlattices, progress in the processing technology let fabricate systems of lower dimensionality such as QWRs where the confinement of the carriers can be controlled through the size and shape of the QWR as well as through the selection of structure and barrier materials to produce various band offsets [163].

Our previous analysis dealing with QWs assumed carrier spatial confinement along one coordinate, where the confinement was provided by the offset between the band edges of two different semiconductors. The next logical step is to consider what happens if carriers are spatially confined along a further direction, leading to 2D confinement (that is one-dimensional free-motion) that defines the kind of nanostructure termed QWR. A semiconductor QWR structure results whenever two characteristic geometric lengths of a semiconductor system are comparable to or smaller than the electronic De Broglie wavelength of the corresponding bulk material. Hence, electron motion is free along the direction of the wire axis (termed x-direction hereafter) and confined along two direction (plane yz of the wire cross-section) (Fig. 3.14). Unlike the case of a QW, different potential profiles (e.g., rectangular and triangular) can be realized in the case of a QWR depending on the fabrication techniques and protocol [164–177]. The role of electron-hole Coulomb interaction also depends on the profile of the confining potential [178, 179].

Different analytical expressions of the confining potential lead to different classes of energy eigenfunctions and may require numerical solving of the Schrödinger equation. Anyway, quantum size effects exhibited by QWRs have general features that can be assessed in the most simple case of a rectangular QWR. Therefore, in the following we will develop the basic theoretical concepts for calculating the electronic and optical properties of QWRs in the case of a rectangular QWR, i.e., electrons (holes) are confined by a square potential well along each of two confinement independent directions (termed y and z hereafter).

In the case of 1D structures, to solve the time-independent Schrödinger equation (Eq. (3.1)) it is possible to decouple the motion along the axis of the QWR (x axis in Fig. 3.14) and the motion along the direction perpendicular (yz plane in Fig. 3.14a). Given the lengths L_x, L_y and L_z (Fig. 3.14), the 2D confinement potential of a rectangular QWR can be decomposed as follows
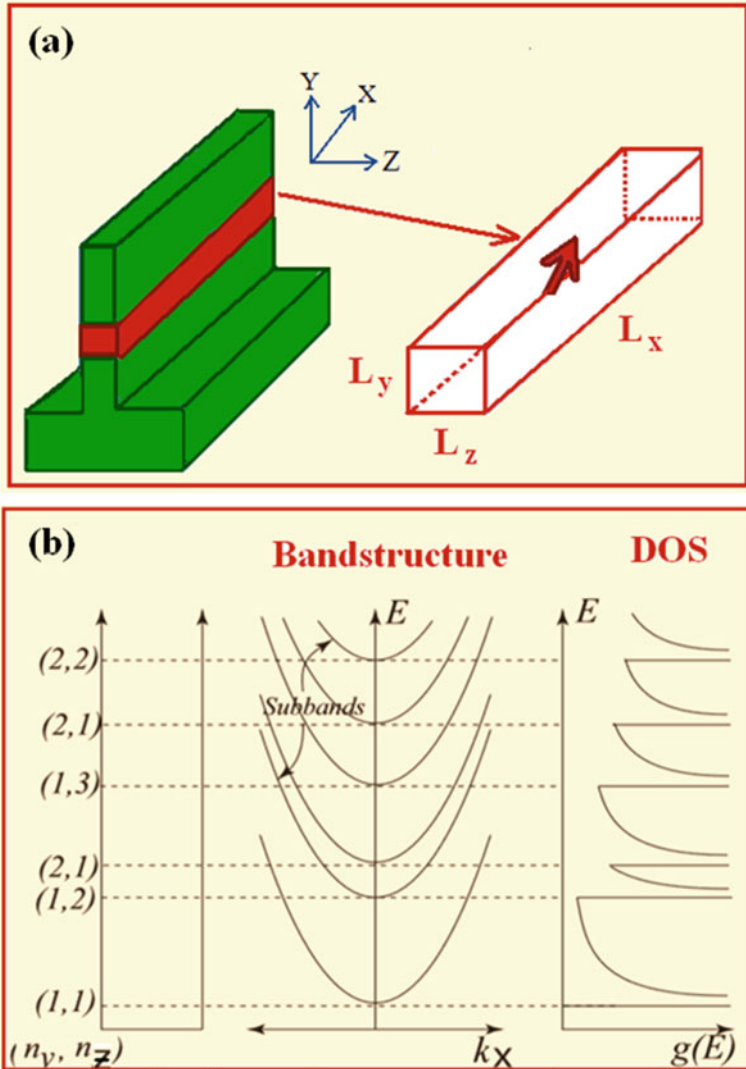
$$V_{QWR}(x, y, z) = V_1(x) + V_{2,3}(y, z)$$

Fig. 3.14 (**a**) Schematics of a QWR heterostructure and corresponding confinement imposed to the electronic motion. (**b**) Bandstructure and DOS of a QWR without excitonic effects

where $V_1(x) = 0$ is the potential ruling the carrier free motion along the wire length (x-axis) and $V_{2,3}$ (y,z) vanishes for $0 < y < L_y$ and $0 < z < L_z$ and is infinite otherwise. Accordingly, the wave function can be written as the following product of wave functions

$$\psi(x, y, z) = \psi^1(x) \; \psi^{2,3}(y, z)$$

Substitution of the above general expression of potential and wave function in the time-independent Schrödinger Eq. (3.1) lets get the following independent Schrödinger equations:

$$\left(-\frac{\hbar^2}{2m_x^*}\frac{\partial^2}{\partial x^2}\right)\psi^1(x) = E^1\psi^1(x)$$

$$\left(-\frac{\hbar^2}{2m_y^*}\left(\frac{\partial^2}{\partial y^2}\right) - \frac{\hbar^2}{2m_z^*}\left(\frac{\partial^2}{\partial z^2}\right) + V_2(y,z)\right)\psi^2(y,z) = E^{2,3}\psi^{2,3}(y,z)$$

where m_x^*, m_y^* and m_z^* is the carrier effective mass along the x, y and z-direction, respectively.

The first Schrödinger equation can be satisfied by a plane wave function

$$\psi^1(x) \approx e^{ik_x \cdot x}$$

and by energy eigenvalues

$$E^1 = \left(\frac{\hbar^2 k_x^2}{2m_x^*}\right)$$

where x is the position along the direction of the QWR axis (free-motion direction) and k_x is the wave vector along the x-axis.

The second Schrödinger equation can be easily solved by observing that in the case of a QWR with rectangular cross-section, geometry lets decouple the dependence on y and z, namely the potential $V_{2,3}$ can be written as $V_{2,3}(y,z) = V_2(y) + V_3(z)$, where $V_2(y) = 0$ if $0 < y < L_y$, $V_2(z) = 0$ if $0 < z < L_z$ and both V_2 and V_3 are infinite otherwise. This approach that separates the variables enables to express

$$\psi^2(y,z) = \psi^2(y)\,\psi^3(z)$$

and

$$E^{2,3} = E^2 + E^3$$

where

$$\left(-\frac{\hbar^2}{2m_y^*}\left(\frac{d^2}{dy^2}\right)\right)\psi^2(y) = E^2\psi^2(y)$$

$$\left(-\frac{\hbar^2}{2m_z^*}\left(\frac{d^2}{dz^2}\right)\right)\psi^3(z) = E^3\psi^3(z)$$

Since the obtained equations to solve are mathematically the Schrödinger equation of an infinite one-dimensional quantum well, eigenfunctions and eivgenvalues are already known. Therefore, under the assumption that L_y and L_z are comparable to the electron De Broglie wavelength in the wire material, it results the following quantized energy spectrum:

$$E^{2,3} = E^2 + E^3 = \left(\frac{\hbar^2}{2m_y^*}\right)\left(\frac{n_y\pi}{L_y}\right)^2 + \left(\frac{\hbar^2}{2m_z^*}\right)\left(\frac{n_z\pi}{z}\right)^2 \text{ where } n_y, n_z = 1, 2, 3, \ldots$$

Therefore, the energy spectrum of a rectangular QWR in the free-electron approximation is given by

$$E_{QWR}^{tot} = E_g + \left(\frac{\hbar^2 k_x^2}{2m_x^*}\right) + \left(\frac{\hbar^2}{2m_y^*}\right)\left(\frac{n_y\pi}{L_y}\right)^2 + \left(\frac{\hbar^2}{2m_z^*}\right)\left(\frac{n_z\pi}{L_z}\right)^2$$

$$\text{where } n_y, n_z = 1, 2, 3, \ldots$$

where E_g is the band gap energy of the bulk material and two quantum numbers, instead of one as in the case of a QW, are now introduced by 2D confinement. In analogy to a QW, a subband forms at each eigenvalue labeled by a couple of quantum numbers (n_y and n_z) with each subband having a free-particle dispersion (i.e., parabolic) as shown by the band structure in Fig. 3.14b. Given the energy dispersion, the resulting DOS has the following expression:

$$g^{QWR}(E) = \frac{1}{\pi}\sqrt{\frac{2m^*}{\hbar^2}}\sum_{n_y n_z}\frac{1}{\sqrt{E - E_{n_y n_z}}}\theta\left(E - E_{n_y n_z}\right)$$

where E_{n_y,n_z} are the confinement energies associated with the y and z directions and the θ function is the Heaviside unit step function The DOS of a QWR has a characteristic inverse square root dependence on the quantized confinement energies leading to the DOS profile shown in Fig. 3.14b. If only the first subband is filled, the system is purely 1D. As more subbands are filled, the system is quasi-1D and the DOS is found by summing over all subbands. The discontinuities in the DOS of a QWR are known as van Hove singularities.

More detailed calculation are reported in the literature to include the effects of the finite barrier height and the validity of the parabolic approximation to represent the valence subbands of a QWR [180, 181]. Notably, in contrast to a QW, where the reduced translational invariance lifts the bulk degeneration of the topmost valence band, the valence subbands of a QWR consist of a weighted linear combination of hh and lh states in such a way that distinction between lh and hh is unjustified in general [182–185]. A consequence of the peculiarities of the dispersion of a QWR is represented by the polarization selection rules accounting for the relative orientation of the polarization of the exciting field with respect to the axis of the QWR. The absorption strength of the hh exciton divided by the absorption strength of the lh exciton, depending on the polarization direction, gives indication of the anisotropy

of the optical matrix elements [185, 186]. In regard to the allowed optical transitions of a QWR, the strength of hh (lh) transitions increases if the polarization of the exciting electric field is parallel (perpendicular) to the wire axis. Besides the valence mixing hh-lh, other quantities influencing the polarization anisotropy are the aspect ratio of rectangular QWRs [185] and the geometry of the cross-section (e.g., square, rectangular, triangular) of the QWR [187].

Because of larger exciton binding energies associated with confinement, as it occurs in QW structures, excitonic effects are expected to be very important in QWRs even at room temperature [188]. Indeed, to interpret the optical spectra of a QWR, the above calculated electron confinement energies must be modified as follows to include excitonic effects:

$$E_{QWR}^{tot} = E_g + \left(\frac{\hbar^2 k_x{}^2}{2m_x^*}\right) + \left(\frac{\hbar^2}{2m_y^*}\right)\left(\frac{n_y \pi}{L_y}\right)^2 + \left(\frac{\hbar^2}{2m_z^*}\right)\left(\frac{n_z \pi}{L_z}\right)^2$$
$$- E_{exc} \text{ where } n_y, n_z = 1, 2, 3, \ldots$$

where E_{ex} is the exciton binding energy. Since a carrier is confined in the wire plane and can move freely along the wire direction of the wire axis, the motion along the wire axis can be separated from the motion in the wire cross-section. The excitonic problem can be solved by introducing relative and center-of-mass coordinates that enable to decouple the starting two-body equation into two one-body equations, as described for a bulk exciton. The sum of the one-particle potentials due to the wire confinement taken at the center-of-mass coordinates is the potential to solve the center-of-mass motion. The relative motion along the wire direction is controlled by the Coulomb interaction.

As discussed in the case of a QW, the exciton binding energy depends on the probability that electron and hole can be found in the same unit cell expressed by the overlap integral of the electron and hole wave functions in the QW. For ideal QW, the binding energy of the ground-state exciton is four times the 3D effective Rydberg. This limit is reached when the well thickness is progressively reduced [136]. Turning from a QW to a QWR, the introduction of an additional confinement direction further enhances the exciton binding energy (by roughly 50 % and depending on the barrier height and degree of non-parabolicity of the valence band) [181]. Large exciton binding energies larger than the ones of QWs of comparable confinement length have been observed in semiconductor wires fabricated by different techniques [189–194]. In a QWR the exciton binding energy is strongly dependent on the spatial extension of the electron and hole wave-functions and theoretically can range from the bulk exciton binding energy to infinity [195–197]. This divergence would suggest that in the ideal 1D limit exciton binding energies can be increased much beyond the 2D limit of a QW [198, 199]. In realistic cases, the exciton binding energy in a QWR is finite and rarely is larger than four times the bulk exciton binding energy. Variational calculations were performed to predict the dependence of the excitonic ground state binding energy on the shape and height of the confining potential in a QWR as well as its scaling with size [200]. It was found a scaling governed by the extension of the

single-particle wavefunctions in the plane perpendicular to the free motion wire direction and much less sensitive to the shape of the wire. Experimental results do not always confirm such a prediction about the dependence on the wire shape [201]. As a general rule, the influence of the excitonic effects on the optical properties of confined systems depends on the size of the confinement length, meaning that if such a length is much larger than the bulk Bohr radius of the exciton a_{ex}^{bulk} then a very weak influence of the confinement is expected (i. e., a weak confinement regime). In detail, for a wide wire ($L_y, L_z > 3\ a_{ex}$) in which the carriers are not confined (L_y, L_z larger than De Broglie wavelength) the excitons feel the boundaries of the wire structure and this involves discrete dispersion of the center of mass motion of the exciton [202, 203]. If $L_y, L_z < 3\ a_{ex}$ then carriers are confined with discrete spectrum (quantization-induced blue-shift of the electronic states) which dominates the optical properties of the QWR and the excitonic motion consists of a purely 1D-confined excitonic motion along the confinement direction and a relative motion along the wire direction controlled by the Coulomb interaction. The reduced dimensionality affects the excitonic wave functions in that the overlap integral of the electron-hole wave functions increases, hence involving enhanced exciton binding energy and oscillator strength of the optical transitions.

Laser operation from GaAs QWRs was first demonstrated in 1989 [204], but then the difficulty in fabricating QWR structures caused relatively slow progress that was further slowed following the discovery that 0D-systems form spontaneously during molecular beam epitaxy (MBE) growth in the Stranski–Krastanow regime [205].

3.3.3 Quantum Confinement in Semiconductor QDs

If carriers are spatially confined down to nanometric scale along all directions, which is the ultimate limit, then 3D confinement results that defines a QD heterostructure. Early synthesis of PbS QDs dates to more than 2000 years ago [206]. More recently, incorporation and tuning of the size and stoichiometry (CdS, CdSe, CuCl and CdSxSe1-x) of QDs in silicate glasses and colloidal solutions was a well assessed trick to change the color of glass [207–209]. In general, semiconductor QDs have been intensively investigated for their unique optical and electrical properties [210, 211] and applications as light emitting devices (LEDs and lasers), coupling QD-(semiconductor/photonic crystal) microcavity systems, solar cells, spintronic devices and biological markers. Fundamental and applicative interest in the potentialities of QDs prompted the development and optimization of processing and growth approaches such as molecular beam epitaxy (MBE) [212], metal-organic chemical-vapor deposition (MOCVD) [213], self organization approaches (QDs fabricated by Volmer-Weber [214] or Stranski-Krastanow [214, 215] growth) and "freestanding" (e.g., colloidal) QDs [216, 217].

Carriers spatially confined in all three coordinates cannot be described by plane-wave eigenstates. In this situation, whenever a characteristic geometric length of the system (e.g., the side for a cubic box or the radius of a spherical particle)

is comparable or smaller than the electronic De Broglie wavelength of the corresponding bulk material, then quantum size effects result. To calculate the energy dispersion of a 0D-system (QD or quantum box) the same general theoretical guidelines developed in the case of QWs and QWRs can be applied. In a simplified model a QD can be assumed to be a box with side L_x, L_y and L_z along the direction x, y and z, respectively (Fig. 3.15a). Under the effective mass approximation of the single-electron model, the electronic states are described by the envelope function satisfying a time-independent Schrödinger equation with infinitely deep potential well along each independent spatial direction (x, y and z) resulting from the potential energy barriers formed at the QD's boundaries. Based on the same arguments applied in the case of a QWR, the 3D confinement potential of a rectangular QD (Fig. 3.15a) can be decomposed as follows

$$V_{QD}(x, y, z) = V_1(x) + V_2(y) + V_3(z)$$

where $V_i(x) = 0$ for $0 < x < L_j$ (where $(i,j) = (1,x), (2,y), (3,z)$) and is infinite otherwise. Accordingly to the method of separable variables, the wave function to be determined can be written as follows

$$\psi(x, y, z) = \psi^1(x) \ \psi^2(y) \ \psi^3(z)$$

Substitution of the above general expression of potential and wave function within the time-independent Schrödinger Eq. (3.1) lets get the following system of three decoupled time-independent Schrödinger equations:

$$\left(-\frac{\hbar^2}{2m_x^*}\left(\frac{d^2}{dx^2}\right)\right)\psi^1(x) = E^1\psi^1(x)$$

$$\left(-\frac{\hbar^2}{2m_y^*}\left(\frac{d^2}{dy^2}\right)\right)\psi^2(y) = E^2\psi^2(y)$$

$$\left(-\frac{\hbar^2}{2m_z^*}\left(\frac{d^2}{dz^2}\right)\right)\psi^3(z) = E^3\psi^3(z)$$

Following the same arguments of QWs and QWRs, the confined energies of a rectangular QD are given as follows

$$E_{n_x n_y n_z} = E^1 + E^2 + E^3 = \left(\frac{\hbar^2}{2m_x^*}\right)\left(\frac{n_x\pi}{L_x}\right)^2 + \left(\frac{\hbar^2}{2m_y^*}\right)\left(\frac{n_y\pi}{L_y}\right)^2 +$$

$$\left(\frac{\hbar^2}{2m_z^*}\right)\left(\frac{n_z\pi}{z}\right)^2 \ (n_x, \ n_y, n_z = 1, 2, 3, \ldots)$$

Schematic representation of the quantum confinement effects of a QD shown in Fig. 3.15c) depicts the changes in the structure of both valence band and conduction
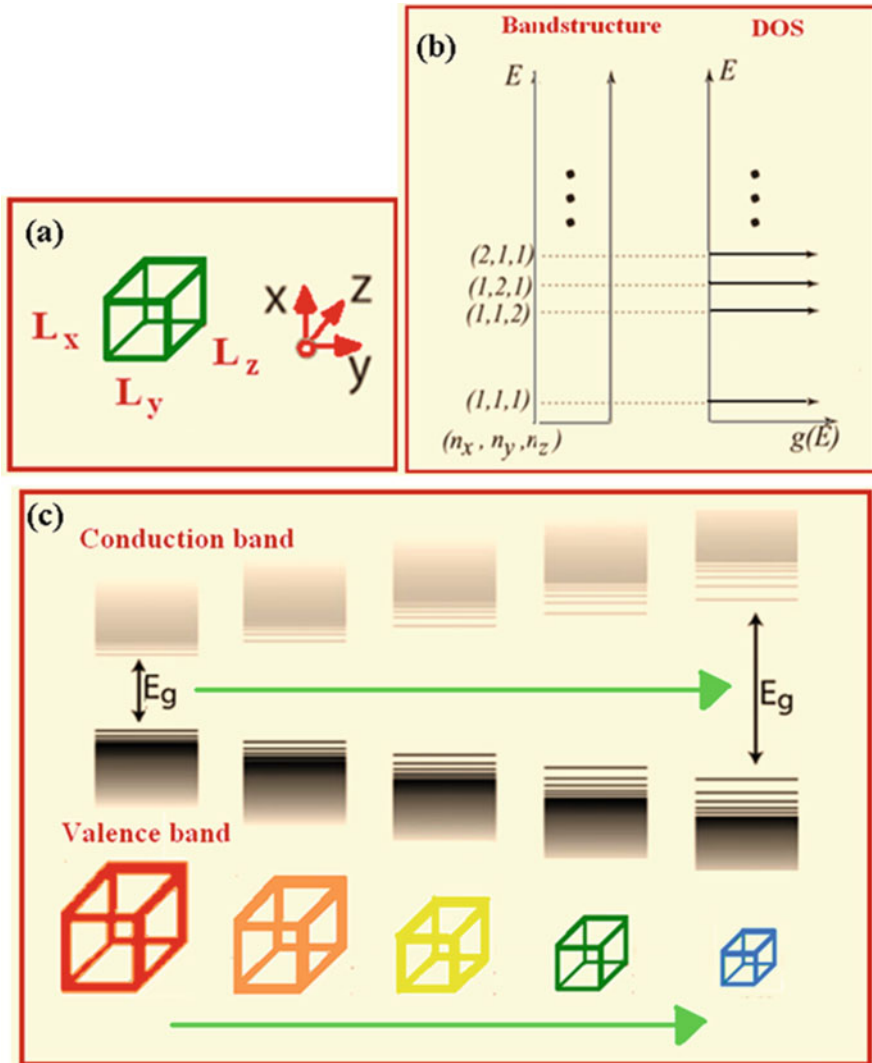
Fig. 3.15 (**a**) Cubic QD and (**b**) corresponding bandstructure and DOS. (**c**) Schematic representation of the quantum confinement effects of a QD: on the structure of both valence band and conduction band: discrete energy states at the band edges of the bulk material with energies and their relative spacing increasing with decreasing size

band: discrete energy states arise at the band edges of the bulk material and such allowed confined energies and their relative spacing increase with decreasing size of the QD [218]. Quantum confinement effects are observed when the QD's size is small enough that the energy level spacing of the confined energies exceeds $k_B T$ (where k_B is Boltzmann's constant and T is the absolute temperature). Typically, the spacing range between QD's intraband energy levels is of 10–100 meV. The carrier

effective mass is important in determining intraband energy spacings too. Notably, the calculated energy spectrum indicates that a QD exhibits distinct narrow optical line spectrum. Parameters involved in the mathematical expression of discrete energy spectrum of a QD indicate that an attractive property of a 0D-system is the possibility to tailor/tune its size, shape and composition for a desired application.

Therefore, the band structure of a QD is a sequence of discrete energy values (atom-like spectrum) (Fig. 3.15b) leading to a DOS given as a series of delta functions

$$g^{QD}(E) = 2 \sum_{n_x n_y n_z} \delta\left(E - E_{n_x n_y n_z}\right)$$

where the factor 2 takes into account the spin degeneracy. This is why QDs are often termed "artificial atoms"(δ-function-like DOS) [219].

In contrast to a QW and a QWR, the DOS of a QD doesn't have at least a piece wise continuous profile, which has an important impact on spectroscopic properties. Indeed, the electron energy spectrum of a QD in the effective mass and free-electron approximations has the following expression:

$$E_{QD}^{tot} = E_g + \left(\frac{\hbar^2}{2m_x*}\right)\left(\frac{n_x \pi}{L_x}\right)^2 + \left(\frac{\hbar^2}{2m_y*}\right)\left(\frac{n_y \pi}{L_y}\right)^2 + \left(\frac{\hbar^2}{2m_z*}\right)\left(\frac{n_z \pi}{z}\right)^2$$

$$\text{where } n_x, \ n_y, n_z = 1, 2, 3, \ldots$$

where E_g is the energy gap of the bulk material and n_x, n_y and n_z are three integer quantum numbers associated to the confinement directions. For example, the energy levels for a cubic QD ($L_x = L_y = L_z$) having side length L and electronic isotropic effective mass ($m_x* = m_y* = m_z* = m_e*$) are

$$E_{QD}^{tot} = E_g + \left(\frac{\hbar^2}{2m_e*}\right)\left(\frac{\pi}{L}\right)^2 \left(n_x^2 + n_y^2 + n_z^2\right) \text{ where } n_x, \ n_y, n_z = 1, 2, 3, \ldots$$

Energy direct transitions from the mth confined energy in the valence band to the nth confined energy in the conduction band are allowed under absorption of incident exciting photons with energy

$$\hbar\omega = E_g + E_n + E_m = E_g + \left(\frac{\hbar^2}{2m_e*}\right)\left(\frac{n\pi}{L}\right)^2 + \left(\frac{\hbar^2}{2m_h*}\right)\left(\frac{m\pi}{L}\right)^2$$

$$(n, m = 1, 2, 3, \ldots)$$

where m_h* is the hole effective mass. Hence, the band gap energy of a cubic QD is given by the above formula by setting $n = m = 1$:

$$E_g^{QD} = E_g + \left(\frac{\hbar^2}{2m_e*}\right)\left(\frac{\pi}{L}\right)^2 + \left(\frac{\hbar^2}{2m_h*}\right)\left(\frac{\pi}{L}\right)^2$$

Such a relationship indicates that the fundamental absorption edge of a QD is larger than the energy gap of the bulk counterpart and blue-shifts with decreasing size of the QD (Fig. 3.15c). The energy gap of a QD also depends on the semiconductor material and its stoichiometry. All of this allows tuning of the energy gap through changes in the QD size, material and composition (doping).

To summarize the key points in the case of a QD (0D system), quantization of the electron and hole spatial motion in any direction has the following implications: (i) quantized energy spectrum mimics the atomic one, (ii) the effective band-edge is blue-shifted; (iii) confinement forces the wave function of electron and hole to overlap, thus favoring the increase of the oscillator strength and probability of radiative transitions; and (iv) the discrete δ-function-like DOS produces narrow optical line spectra. Points (i) and (iv) justify the nomenclature "artificial atoms" adopted to describe the peculiar spectroscopy behavior of QD systems (Fig. 3.16a). Based on the delta-like DOS, the optical spectrum of a QD would be expected to consist of spectrally narrow emission characteristics. Instead, the conventional spectroscopic measurements of QDs reveal emission spectra with significantly broadened peaks [220–225]. This experimental evidence can be attributed to the fact that conventional procedures acquire the emission response of an ensemble of QDs rather than of a single QD. Hence, spectroscopy of single QDs is the starting point to understand and evaluate their intrinsic physical properties but, in practice, it is not possible to describe a QD ensemble/array by the spectroscopy of a single QD. In fact, fluctuations of size and shape ("regularly shaped" QDs require excellent growth conditions!) as well as compositional non-uniformities involve spectral inhomogeneous broadening of the spectral lines. Indeed, real samples consist of a distribution of QDs polydispersed in size and shape. If several families $i = 1,\ldots,N$ of QDs with dimension $R_i \pm \Delta R_i$ concur to the emission spectrum of a QD-based system, then the observed emission spectrum reflects the convolution of all the emission spectra resulting from each family of QDs composing the sample (Fig. 3.16b). Therefore, fabrication techniques are crucial to ensure structural quality of the samples avoiding strong inhomogeneous broadening of the absorption/emission features. Extremely high spatial resolution imaging tools can help in probing the optical response of a single QD and disclose its atom-like behavior [219, 222, 226].

Furthermore, spectroscopic properties of QDs cannot be correctly interpreted without taking into account the excitonic effects that often play a dominant role because of further increased binding energy of an exciton in a QD as compared to QWs and QWRs. Optical transitions in QDs can be described by an approximated expression (known as the Brus equation) that models the transition energy in spherical QDs with radius R and relative dielectric constant ε_r (QD with dielectric coefficient ε_{QD} surrounded by a medium of dielectric coefficient ε_m):

$$E_g^{QD} = E_g + \left(\frac{\hbar^2\pi^2}{2R^2}\right)\left(\frac{1}{m_e{}^*} + \frac{1}{m_h{}^*}\right) - \left(\frac{1.8\,q^2}{4\pi R \in_r \in_o}\right)$$
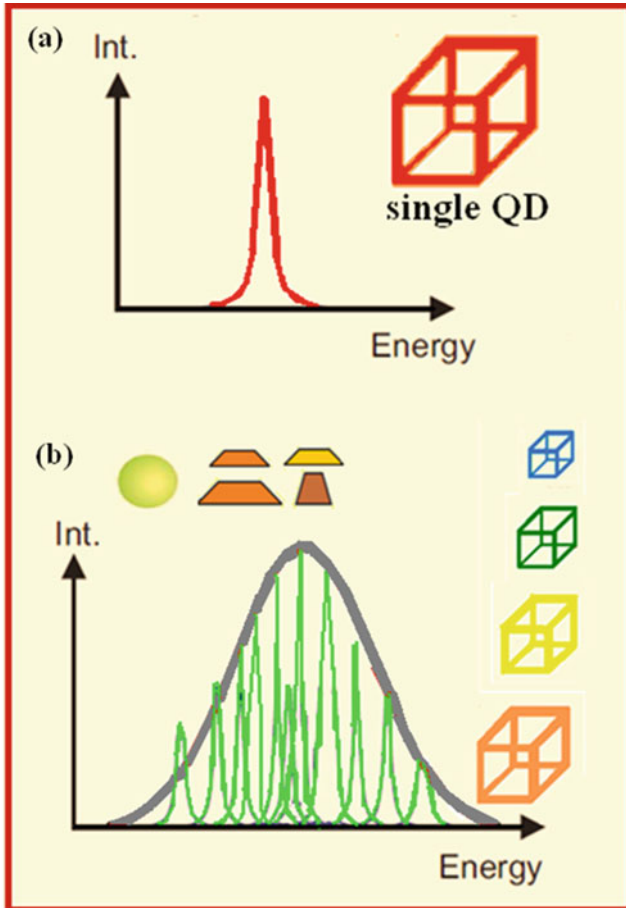
Fig. 3.16 (**a**) Emission spectrum of (a) a single QD and (**b**) a distribution of QDs with size and shape dispertion

In the Brus equation ε_o is the permittivity of vacuum and ε_r is the relative dielectric constant of the sherical QD that confines an exciton. The third term is related to the electron-hole Coulomb attraction and express the binding energy of the exciton which is influenced from the size R of the QD due to quantum confinement [227].

As described earlier, in bulk semiconductors, excitons are observable typically only at very low temperatures because room temperature thermal energy can easily dissociate the exciton. Instead, in quantum confined structures, a closer spacing between electron and hole enhances the excitonic binding energy (the exciton feels the confinement boundaries even if the confining well is larger than the exciton bulk Bohr radius) that turns out to be more enhanced and stable at room temperature the larger the number of confining directions. In a QD the exciton binding energy is

strongly dependent on the spatial extension of the electron and hole wave-functions and, even if theoretically can range from the bulk exciton binding energy to infinity, in practice it rarely exceeds 4 times the bulk exciton binding energy.

Since in a bulk semiconductor crystal the exciton Bohr radius (a_{ex}^{bulk}) is significantly smaller than the overall size of the crystal, the exciton is free to migrate throughout the lattice. Instead, weak confinement (i.e., the confinement length L is slightly larger than or comparable to a_{ex}^{bulk}) and strong confinement (i.e., the confinement length L is much smaller than a_{ex}^{bulk}) regimes can be introduced at the mesoscopic scale [228]. In the case of weak confinement the exciton binding energy is larger than the carrier quantization energy and, in presence of quantum confinement, exciton forms with center-of-mass motion localized and quantized. Coulomb interaction can be treated as a perturbation to the QD confinement potential for electrons and holes and the exciton binding energy can be calculated based on the perturbation theory as follows

$$E_B \approx \frac{e^2}{\varepsilon_r} \iint d\mathbf{r}_e d\mathbf{r}_h \frac{|U_e(\mathbf{r}_e) U_h(\mathbf{r}_h)|^2}{|\mathbf{r}_e\text{-}\mathbf{r}_h|}$$

where $U_e(\mathbf{r_e})$ and $U_h(\mathbf{r_h})$ are electron and hole wave-functions.

Strong confinement involves the exciton binding energy is smaller than the confinement energy of the carriers and confinement effects dominate over the Coulomb ones, thus leading to electron-hole states with dominant single-particle character. That is, carriers do not form bond states corresponding to the exciton (electrons and holes are separately confined) and wave function can be represented as a product of electron and hole wave-functions $\psi = U_e(\mathbf{r_e}) U_h(\mathbf{r_h})$, where the single-particle wave-functions are solutions of coupled Schrödinger equations with the QD potential for an electron (a hole) $V_{e,h}$

$$\left(-\frac{\hbar^2}{2m^*_{e,h}} \nabla^2_{e,h} + V_{e,h} - \frac{e^2}{\varepsilon_r} \int d\mathbf{r}_{h,e} \frac{|U_{h,e}(\mathbf{r}_{h,e})|^2}{|\mathbf{r}_e\text{-}\mathbf{r}_h|} \right) U_{e,h}(\mathbf{r}_{e,h}) = E_{e,h} U_{e,h}(\mathbf{r}_{h,e})$$

In this case, the exciton binding energy is defined by

$$E_B^{QD} = E_e^o + E_h^o - E_e - E_h$$

where E_e^o and E_h^o are energies of electron and holes that do not interact by Coulomb coupling.

In semiconductor QDs singly and multiply charged excitons were studied by photoluminescence spectroscopy applied to a single QD [229–232].

More generally, the bulk exciton Bohr radius (a_{ex}^{bulk}) is taken as the measure of quantum confinement in low-dimensional systems: given a solid state structure with characteristic length R:

(i) if $R \gg a_{ex}^{bulk}$, then confinement effects are generally negligible;
(ii) if $R > a_{ex}^{bulk}$ or $R \sim a_{ex}^{bulk}$, then the weak confinement regime occurs;
(iii) if $R < a_{ex}^{bulk}$, then we the strong confinement regime occurs.
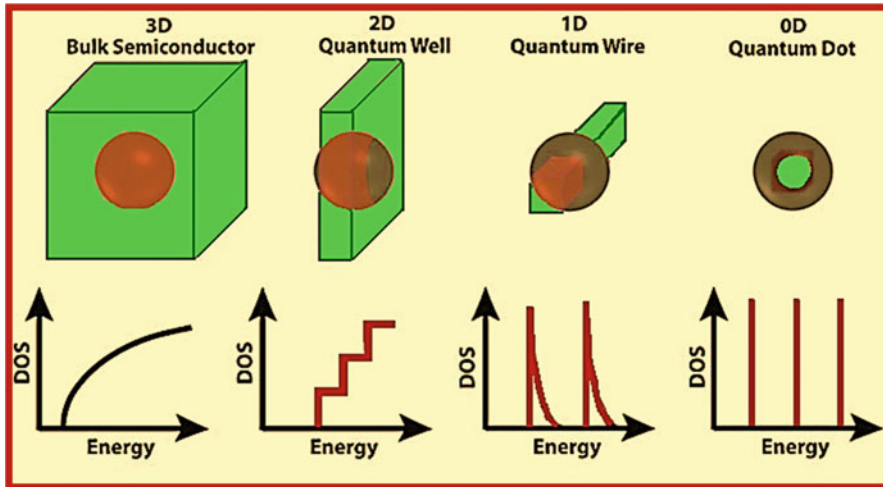
Fig. 3.17 Schematic overview of the DOS of semiconductor nanostructures (2D, 1D and 0D structures) in the excitonic strong confinement regime

A schematic overview of the DOS of semiconductor nanostructures (2D, 1D and 0D structures) in the strong confinement regime is shown in Fig. 3.17 [233]. For comparison the case of the bulk semiconductor (3D case) is also depicted and the exciton Bohr diameter is represented by a dark sphere.

Another important role in interpreting the optical properties of QDs is played by the electronic quantum states associated with the surface (called surface states) due to the high surface-to-volume ratio of mesoscopic systems [234, 235]. High density of surface sites associated with high surface-to-volume ratio may cause an enhanced or reduced transfer rate of photogenerated charge carriers (electron or hole or exciton) by their trapping and behaving as reducing (electron) or oxidizing (hole) agents [236, 237]. Capping or passivation (i.e., saturation of surface dangling bonds) of the QD's surface lets provide photostable QDs whenever surface states are detrimental because of their quenching radiative recombination and reducing the quantum yields.

3.4 Quantum Effects in Metal Nanoparticles

As already pointed out, the Fermi wavelength is the smallest length scale associated with confinement effects in metal nanostructures, that is properties become size-dependent when the geometrical size of the metal structure is comparable to or smaller than the Fermi wavelength. Since the conduction electron density is larger in metals than in semiconductors, the Fermi wavelength is of the order of a few nanometers in metals and tens of nanometers in semiconductors. A consequence of very short Fermi wavelength in metals is that confinement effects may be observed

in metal nanostructures only at size-scales of a few nanometers. The optical, electromagnetic properties of metal nanoparticles remarkably differ from bulk materials [23, 29, 35]. At the nanometric length-scale, for size larger than a few nanometers (tipically larger than 10 nm) the optical properties of metallic nanoparticles are governed by the so called surface plasmon resonance that disappears with decreasing size. Indeed, the electronic structure of metal nanoclusters/nanoparticles exhibits an important nanoparticle phenomenon known as "surface plasmon resonance" (SPR) or localized surface plasmon resonance (LSPR), that is a coherent collective charge oscillation of the conduction band electrons at the interface between conductors and dielectrics induced by an external electromagnetic field with frequency matching the plasma frequency of the metal [22–28, 238]. For example gold nanoparticles show a strong absorption band in the visible region due to coupling through the surface between surface plasmon oscillation modes of conduction electrons and the applied electromagnetic field. The oscillation frequency is determined by the density of electrons, the electron mass, the size, and the shape of the charge distribution. At the fundamental level, the free electrons of a metal are modeled like a gas of free charge carriers (a so-called plasma) and can be excited to sustain propagating plasma waves, that is longitudinal electromagnetic charge density waves, whose quanta are termed "plasmons". Plasmons exist in the form of both bulk plasmons in the volume of a plasma and surface plasmons bound to the interface between a plasma and a dielectric. When the size of a metal nanoparticle is in the range of the penetration depth of an electromagnetic field into the metal (e.g., ∼20 nm for silver in the optical spectral range), there is no distinction between surface and bulk plasmons.

The first example of this nanoscale phenomenon dates to some glassblowers from imperial Rome made by embedding colloidal metal nanoparticles within glassy works. Another well-known fine example is the famous Lycurgus Cup (fourth century A.D.): such a chalice has a dark greenish tint under reflected lighting and appears red once illuminated from behind. Some of the beautiful bright colors in medieval stained glass windows are a metal-nanoparticle phenomenon that fascinated scientists long before studies of semiconductors and was explained later when Faraday (1857) proposed metallic gold in its colloidal form as origin of colorful emission and Mie (1908) [239] provided the theoretical foundations for understanding the physical behavior and optical responses of metal nanoparticles by solving Maxwell's equation for the absorption and scattering of electromagnetic radiation by spherical particles ($2R \ll \lambda$, being λ the wavelength of the light irradiating the particle with radius R). On the basis of Mie theory, the plasmon band of metal particles involves electric-field induced dipolar oscillations of the free electrons in the conduction band that occupy energy states near the Fermi level.

Essentially, bright colors can be observed from colloidal solutions of metallic nanoparticles with their color emission tunable by changing shape, size, composition, orientation and local dielectric environment of the nanostructures [240, 241]. In what concerns the comparison between the optical properties of semiconductor QD [242] and metal nanoparticles [243] as a function of size and shape, it can be observed that while the optical spectra of semiconductor QDs are very sensitive to changes in size (due to the already discussed confinement energies which scale as the inverse of the squared radius), instead just a slight change and a drastic change

of the optical response can be observed in the case of metal nanoparticles versus size and shape changes, respectively. Therefore, metal nanoparticles are more sensitive to anisotropy than to size tuning. Introducing an anisotropy (for example a shape transition from sphere to rod by femtosecond laser irradiation of colloidal metal nanoparticles) results in the splitting of the SPR into two modes. Also, an increase in the refractive index of the dielectric surrounding a metal nanoparticle leads to a red-shift of the surface plsmon resonance peak as well to an increase in the plasmon band intensity and bandwidth. The shift if the SPR peak caused by changes in the local environment (such as adsorbed species or a core-shell structure) within a distance d around the nanoparticle can be calculated by $\Delta\lambda_{max} = n\,\Delta n[1-\exp(-2d/l_d)]$, where n is the bulk refractive-index response of the nanoparticle(s); Δn is the change in refractive index induced by the surrounding and l_d is the characteristic exponential decay length of the electromagnetic field [244, 245]. In the case of a metal-core/shell structure of the nanoparticle, thickening of the shell embedding the nanoparticle can cause a blue-shift or a red-shift of the SPR peak depending on the shell composition [246–248].

Under resonant excitation of metal nanoparticles, an enhancement of the local electric fields close to the particle surface occurs. Enhancement and local SPR dependency on size and shape indicate that the smallest nanoparticles have a maximum SPR peak at shorter wavelengths [249, 250], too small nanoparticles exhibit reduced effective conductivity and light scattering [251], for nanoparticle size of the order of the exciting wavelength non radiative modes become favoured [251] and shapes with high curvature corners and edges strongly enhance the local field around these geometrical features [252, 253].

Scaling down to dimensions of a few nanometers removes the SPR from the optical properties of the metal nanostructures and enables to observe a shift in the conductive properties from metallic to semiconducting and insulating with progressively decreasing size. The origin of such a modified electronic structure of metals at very small scale-lengths is the discreteness of the electronic states due to confinement of the electron wavefunction. As the nanoparticle size decreases, the energy continuum of the bulk metal transforms into discrete energy levels (Fig. 3.18). The average spacing of successive quantum levels, δ, is termed the Kubo gap and is given by $\delta = 4E_F/3\,N$, where E_F is the Fermi energy of the bulk material and N is the nuclearity (number of atoms in the metal nanocluster), which is related to the number of valence electrons in the metal [30–32]. In this picture, metallic behavior is ascribed to gap between occupied and unoccupied electronic states at the Fermi level vanishing (bulk metal) or smaller than the thermal energy k_BT (metal nanoparticle) (Fig. 3.18). For scaling size from bulk to nano-scale metal the Kubo gap increases because the number of atoms decreases. Therefore, for decreasing size (and/or temperature) a threshold is reached when the Kubo gap equals the thermal energy k_BT. In this circumstance a transition/shift in conductive properties, from metallic to semiconducting/insulating behavior, results. Based on a well-known mechanism applied in semiconductor solid-state physics, when electrons can be thermally excited across the Kubo gap, a low temperature insulator becomes a semiconductor and a metal at higher temperatures. According to the principles of band theory, the overlapping between atomic orbitals of neighboring atoms
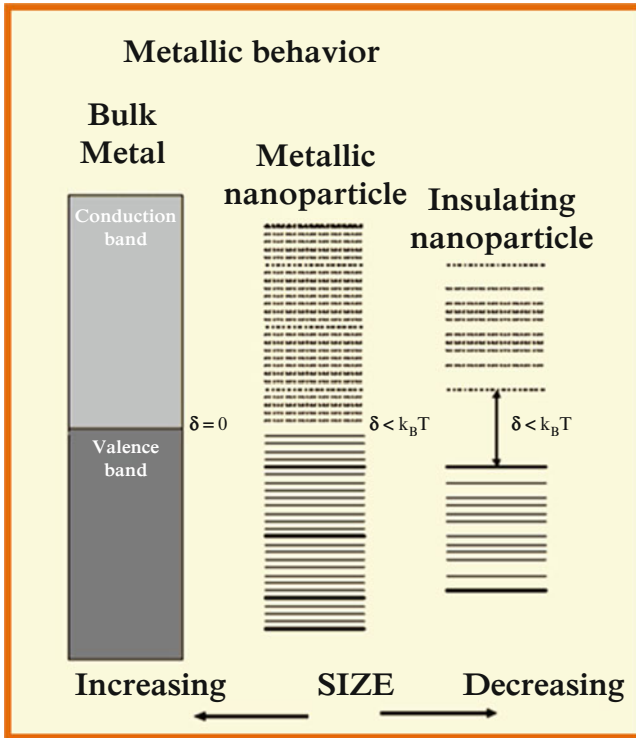
Fig. 3.18 Changes of the electronic structure of metals going from the bulk phase to the nanoscale (a few nanometers) where the plasmonic resonance disappears and discrete energy spectrum accounts for the metal-to-insulator conductivity transition

leads to bonding and antibonding states, namely valence and conduction bands in semiconductors, with a band width related to the bond strength. Hence, the insulating properties of nanometric metal systems can be ascribed to the small number of neighboring atoms. Indeed, in the case of systems consisting of a relatively poor number of atoms (e.g., nanoparticles with size of a few nanometers), weak non metallic interactions (e.g., van der Waal forces) hold together the atom constituents and no band may form.

3.5 Summary and Conclusions

Since the famous Feynman's lecture, titled "There's Plenty of Room at the Bottom", regarding the challenging applicative perspectives for nanomaterials and the first use of the term "nanotechnology" by Taniguchi, there has been a widespread interest devoted to nanomaterials at both fundamental and applicative level.

While the fundamental behavior of bulk materials is inherently determined by structure and composition, at the nanometer length-scale fascinating effects and phenomena occur strictly related to either spatial confinement of the electronic wavefunctions or surface-effects.

This review paper has introduced and discussed the fascinating fundamental properties of nanomaterials by treating the meaning of quantum confinement, the importance of the surface effects and their technological applications, the classification usually adopted to refer to the low-dimensional systems, the quantum models applied to solve for both electronic and excitonic dispertion of the mesoscopic semiconductor systems and the nanoscale behavior of the metal nanoparticles.

The developed discussion has pointed out the following main different behaviors of the nanoworld as compared to the 3D bulk world.

In regard to the confinement effects, when at least one of the material dimensions L is comparable with the De Broglie electronic wavelength of the corresponding bulk band-gap material, then the energy spectrum becomes quantized along the confinement direction. Such phenomenon, termed "quantum size effect" involves a larger band gap and a blue shift of the absorption onset with decreasing size as compared of the bulk counterpart as well as material optical properties tunable as a function of both the confinement dimension L and number of the confinement directions.

Moreover, whenever the length scale of the material is comparable to the wavelength of the phonons, discrete phonon density of states form too. Since electron-phonon interaction determines the thermal conductivity and affects carrier dynamics in quantum-confined systems, different thermalization rules and processes (multiphonon processes, Coulomb interactions and phonon-bottleneck effects) occur in nanomaterials as compared to the bulk counterpart due to discrete density of states.

In the case of metallic nanoclusters/nanoparticles, for which there is no band-gap between valence and conduction bands, another phenomenon known as *plasmon resonance* is active, involving localized enhancement of the field intensity with important applicative perspectives in bio-imaging and sensing. For metallic nanoclusters with dimensions smaller than 2 nm, the surface plasmon absorption disappears: the spacings between adjacent energy levels (referred to as the *Kubo* gap) become comparable to the thermal energy, k_BT, resulting in a shift in the conductive properties from metallic to semiconducting and insulating with decreasing size.

Among the technological important behaviors of nanomaterials, pre-melting and lowered melting temperature as compared to the bulk counterpart are very recently active research topics which are ascribed to surface effects such as the increased fraction of surface atoms and surface curvature with decreasing size. Lowered melting temperature may occur for isolated and un-supported nanomaterials. In fact, nanocrystals embedded in a matrix can melt below or above the melting point of the corresponding bulk crystal depending on the interface structure between embedded nanocrystals and the matrix. If the interfaces are coherent or semi-coherent, an enhancement of the melting point is present. Otherwise, there is a depression of the melting point.

Amazing thermal behavior is also exhibited by nanofluids, which can exhibit substantial increment of the thermal conductivity even when the concentrations of suspended nanoparticles are very low, and the more enhanced the smaller nanomaterial size. The thermal conductivity of nanofluids varies with the size, shape, and material of nanoparticles as well as difference of thermal conductivity between nanomaterial and base fluid.

On the other hand, the evidence of quantum size effects make the Plank's blackbody model unable to describe the thermal emission spectrum at the nanoscale (at particle dimensions smaller than the radiation wavelength), where the Stefan–Boltzmann law yields strongly overestimated results.

Furthermore, the catalysis and magnetic properties of nanomaterials strongly differ as compared to the bulk materials. As can example, superparamagnetism is a form of magnetism peculiar of ferromagnetic or ferromagnetic nanomaterials.

Efforts of science and technology are presently focused on understanding the origin of the mechanical, chemical, reactivity, catalysis, thermal, electrical, optical, magnetic properties of nanomaterials, which strongly differ from the bulk counterpart, as well as being able to engineer and control shape and size, size- and shape- dispersion as well as composition at the nanoscale.

The huge amount of studies and papers about nanomaterials published in the last decades and still presently demonstrates that the interest in this research field is growing more and more. What do you expect?. Very likely further fundamental surprising properties as well as challenging opportunities and novel applications made possible by improved nanofabrication approaches and nanostructuring.

References

1. Feynman, R. (1992). There's plenty of room at the bottom. *Journal Microelectromechanical Systems, 1*, 60–66.
2. Taniguchi, N. (1974). On the basic concept of 'Nano-Technology, Proc. Intl. Conf. Prod. Eng. Tokyo, Part II, Japan Society of Precision Engineering.
3. McMullan, D. (1995). Scanning electron microscopy 1928–1965. *Scanning, 17*(3), 175–185.
4. Smith, K. C. A., & Oatley, C. W. (1955). The scanning electron microscope and its fields of application. *British Journal of Applied Physics, 6*(11), 391–399.
5. Zaefferer, S. (2011). A critical review of orientation microscopy in SEM and TEM, Crystal Research and Technology. *New Developments in Electron Diffraction, 46*, 607–628.
6. Williams, D. B., & Carter, C. B. (2009). *Transmission electron microscopy, a textbook for materials science* (2nd ed.). New York: Springer-Verlag.
7. Binnig, G., Rohrer, H., Gerber, C., & Weibel, E. (1982). Surface studies by scanning tunneling microscopy. *Physical Review Letters, 49*, 57–61.
8. Giaever, I. (1960). Energy gap in superconductors measured by electron tunneling. *Physical Review Letters, 5*, 147–148.
9. Binnig, G., Quate, C. F., & Gerber, C. (1986). Atomic force microscope. *Physical Review Letters, 56*, 930–933.
10. Synge, E. H. (1928). A suggested method for extending microscopic resolution into the ultra-microscopic region. *Philosophical Magazine, 6*, 356–362.

11. Betzig, E., Trautman, J. K., Harris, T. D., S: Weiner, J., & Kostelak, R. L. (1991). Breaking the diffraction barrier: Optical microscopy on a nanometric scale. *Science, 251*, 1468–1470.
12. Abbe, E. (1873). Beiträge zur theorie des mikroskops und der mikroskopischen wahrnehmung. *Archiv für mikroskopische Anatomie, 9*, 413–468.
13. Stroscio, M. A., & Dutta, M. (2001). *Phonons in nanostructures*. New York: Cambridge University Press.
14. Liu, G. K., Zhuang, H. Z., & Chen, X. Y. (2002). Restricted phonon relaxation and anomalous thermalization of rare-earth ions in nanocrystals. *Nano Letters, 2*, 535–539.
15. Meltzer, R. S., & Hong, K. S. (2000). Electron-phonon interactions in insulating nanoparticles: Eu_2O_3. *Physical Review B, 61*, 3396–3496.
16. Tamura, A. (1995). Smoothed density of states of electrons and smoothed frequency spectrum of phonons for a mesoscopic system. *Physical Review B, 52*, 2688–2676.
17. Collins, J. (2016). Non-radiative processes in crystals and in nanocrystals. *ECS Journal of Solid State Science and Technology, 5*(1), R3170–R3184 and references therein.
18. Heitz, R., Grundmann, M., Ledentsov, N. N., Eckey, L., Veit, M., Bimberg, D., Ustinov, V. M., Egorov, A. Y., Zhukov, A. E., Kopev, P. S., & Alferov, Z. I. (1996). Multiphonon-relaxation processes in self-organized InAs/GaAs quantum dots. *Applied Physics Letters, 68*, 361–363.
19. Raymond, S., Fafard, S., Charbonneau, S., Leon, R., Leonard, D., Petroff, P. M., & Merz, J. L. (1995). Photocarrier recombination in $Al_yIn_{1-y}As/Al_xGa_{1-x}As$ self-assembled quantum dots. *Physical Review B, 52*, 17238–17242.
20. Efros, A. L., Kharchenko, V. A., & Rosen, M. (1995). Breaking the phonon bottleneck in nanometer quantum dots: Role of Auger-like processes. *Solid State Communications, 93*, 281–284.
21. Benisty, H., Sotomayor-Torres, C. M., & Weisbuch, C. (1991). Intrinsic mechanism for the poor luminescence properties of quantum-box systems. *Physical Review B, 44*, 10945–10948.
22. Otto, A. (1968). Excitation of nonradiative surface plasma waves in silver by the method of frustrated total reflection. *Zeitschrift fur Physik A: Hadrons and Nuclei, 216*, 398–410.
23. Novotny, L., & Hecht, B. (2006). *Principles of nano-optics* (pp. 378–393). Cambridge: Cambridge University Press.
24. Fan, X., Zheng, W., & Singh, D. J. (2014). Light scattering and surface plasmons on small spherical particles (review). *Light: Science & Applications, 3*, e179. doi:10.1038/lsa.2014.60.
25. Homol, J., Yee, S. S., & Gauglitz, G. (1999). Surface plasmon resonance sensors: Review. *Sensors and Actuators B: Chemical, 54*, 3–15.
26. Willets, K. A., & Van Duyne, R. P. (2007). Localized surface plasmon resonance spectroscopy and sensing. *Annual Review of Physical Chemistry, 58*, 267–297.
27. Bohren, C. F., & Huffman, D. R. (1983). *Absorption and scattering of light by small particles*. New York: Wiley.
28. Kreibig, U., & Vollmer, M. (1995). *Optical properties of metal clusters*. Berlin: Springer.
29. Warnes, W. L., Dereux, A., & Bobesen, T. W. (2003). Surface plasmon subwavelength optics. *Nature, 424*, 824–830.
30. Ghosh, S. K. (2011). Kubo gap as a factor governing the emergence of new physicochemical characteristics of the small metallic particulate. *Assam University Journal of Science & Technology: Physics & Science Technology, 7*, 114–121.
31. Kubo, R. (1962). Electronic properties of metallic fine particles. I. *Journal of the Physical Society of Japan, 17*, 975–986.
32. Kubo, R., Kawabata, A., & Kobayashi, S. (1984). Electronic properties of small particles. *Annual Review of Materials Science, 14*, 49–66.
33. Campion, A., & Kambhampati, P. (1998). Surface-enhanced Raman scattering. *Chemical Society Reviews, 27*, 241–250.
34. Sharma, B., Cardinal, M. F., Kleinman, S. L., Greeneltch, N. G., Frontiera, R. R., Blaber, M. G., Schatz, G. C., & Van Duyne, R. P. (2013). High-performance SERS substrates: Advances and challenges. *MRS Bulletin, 38*, 615–624.

35. Nie, S., & Enmory, S. R. (1997). Probing single molecules and single nanoparticles by surface-enhanced. *Science, 275*, 1102–1106.
36. Jankiewicz, B. J., Jamiola, D., Choma, J., & Jaroniec, M. (2012). Silica–metal core–shell nanostructures. *Advances in Colloid and Interface Science, 170*, 28–47.
37. Biener, J., Wittstock, A., Baumann, T. F., Weissmüller, J., Bäumer, M., & Hamza, A. V. (2009). Surface chemistry in nanoscale materials. *Materials, 2*, 2404–2428.
38. Pawlow, P. (1909). The dependency of the melting point on the surface energy of a solid body. *Zeitschrift für Physikalische Chemie, 65*, 545–548.
39. Takagi, M. (1954). Electron-diffraction study of liquid-solid transition of thin metal films. *Journal of the Physical Society of Japan, 9*, 359–363.
40. Goldstein, A. N., Echer, C. M., & Alivisatos, A. P. (1992). Melting in semiconductor nanocrystals. *Science, 256*, 1425–1427.
41. Buffat, P., & Borel, J.-P. (1976). Size effect on the melting temperature of gold particles. *Physical Review A: Atomic, Molecular, and Optical Physics, 13*, 2287–2298.
42. Sar, D. K., Nayak, P., & Nanda, K. K. (2008). Thermodynamic model for the size-dependent melting of prism-shaped nanoparticles. *Physics Letters A, 372*, 4627–4629.
43. Qi, W. H. (2005). Size effect on melting temperature of nanosolids. *Physica B, 368*, 46–50.
44. Sun, C. Q., Wang, Y., Tay, B. K., Li, S., Huang, H., & Zhang, Y. B. (2002). Correlation between the melting point of a nanosolid and the cohesive energy of a surface atom. *The Journal of Physical Chemistry. B, 106*, 10701–10705.
45. Bachels, T., Guntherodt, H. J., & Schafer, R. (2000). Melting of isolated tin nanoparticles. *Physical Review Letters, 85*, 1250–1253.
46. Zhang, M., Efremov, M. Y., Schiettekatte, F., Olson, E. A., Kwan, A. T., Lai, S. L., Wisleder, T., Greene, J. E., & Allen, L. H. (2000). Size-dependent melting point depression of nanostructures: Nanocalorimetric measurements. *Physical Review B, 62*, 10548–10557.
47. Wang, X.-Q., & Mujumdar, A. S. (2007). Heat transfer characteristics of nanofluids: A review. *International Journal of Thermal Sciences, 46*, 1–19.
48. Planck, M. (1901). Ueber das Gesetz der Energieverteilung in Normalspectrum. *Annalen der Physik, 4*, 553–563.
49. Martynenko, Y. W., & Ognev, L. I. (2005). Thermal radiation from nanoparticles. *Technical Physics, 50*, 1522–1254.
50. Wuttke, C., & Rauschenbenbeutel, A. (2013). Thermalization via heat radiation of an individual object thinner than the thermal wavelength. *Physical Review Letters, 111*(1–5), 024301.
51. Kolhatkar, A. G., Jamison, A. C., Litvinov, D., Willson, R. C., & Lee, T. R. (2013). Tuning the magnetic properties of nanoparticles. *International Journal of Molecular Sciences, 14*, 15977–16009.
52. Issa, B., Obaidat, I. M., Albiss, B. A., & Haik, Y. (2013). Magnetic nanoparticles: Surface effects and properties related to biomedicine applications. *International Journal of Molecular Sciences, 14*, 21266–21305.
53. Ashcroft, N. W., & Mermin, N. D. (1976). *Solid state physics*. New York: Holt/Rineheart/Winston.
54. Kasap, S. O. (2002). *From principles of electronic materials and devices* (2nd ed.). Boston: McGraw-Hill.
55. Frenkel, Y. I. (1936). On the solid body model of heavy nuclei. *Phys. Z. Soviet Union, 9*, 158–186.
56. Wannier, G. H. (1937). The structure of electronic excitation levels in insulating crystals. *Physics Review, 52*, 191–197.
57. Mott, N. F. (1938). Conduction in polar crystals. II. The conduction band and ultra-violet absorption of alkali-halide crystals. *Transactions of the Faraday Society, 34*, 500–506.
58. Knox, R. S. (1963). *Theory of excitons*. New York: Academic Press.
59. Bassani, F., & Pastori Parravicini, G. (1975). *Electronic states and optical transitions in solids*. Oxford: Pergamon Press.

60. Koch, W., Kira, M., Khitrova, G., & Gibbs, H. M. (2006). Semiconductor excitons in new light. *Nature Materials, 5*, 523–531.
61. Haug, H., & Koch, S. W. (2006). In H. Haug & S. Koch (Eds.), *Quantum theory of the optical and electronic properties of semiconductors* (4th ed.). Singapore: World Scientific.
62. Nakajima, A., Futatsugi, T., Kosemura, K., Fukano, T., & Yokoyama, N. (1999). Si single-electron tunneling transistor with nanoscale floating dot stacked on a Coulomb island by self-aligned process. *Journal of Vacuum Science & Technology, 17*, 2163–2171.
63. Leobandung, E., Guo, L., Wang, Y., & Chou, S. Y. (1995). Observation of quantum effects and Coulomb blockade in silicon quantum-dot transistors at temperatures over 100 K. *Applied Physics Letters, 67*, 938–940.
64. Pikus, F. G., & Likharev, K. K. (1997). Nanoscale field-effect transistors: An ultimate size analysis. *Applied Physics Letters, 71*, 3661–3663.
65. Zhang, S. K., Zhu, H. J., Lu, F., Jiang, Z. M., & Wang, X. (1998). Coulomb charging effect in self-assembled Ge quantum dots studied by admittance spectroscopy. *Physical Review Letters, 80*, 3340–3343.
66. Ishikuro, H., Fujii, T., Saraya, T., Hashiguchi, G., Hiramoto, T., & Ikoma, T. (1996). Coulomb blockade oscillations at room temperature in a Si quantum wire metal-oxide-semiconductor field-effect transistor fabricated by anisotropic etching on a silicon-on-insulator substrate. *Applied Physics Letters, 68*, 3585–3587.
67. Hanna, A. E., & Tinkham, M. (1991). Variation of the Coulomb staircase in a two-junction system by fractional electron charge. *Physical Review B, 44*, 5919–5922.
68. Grabert, H. (1991). Single charge tunneling: A brief introduction. *Zeitschrift fur Physik B: Condensed Matter, 85*, 319–325.
69. Kim, K. (1998). Visible light emissions and single-electron tunneling from silicon quantum dots embedded in Si-rich SiO_2 deposited in plasma phase. *Physical Review B, 57*, 13072–13076.
70. Wilkins, R., Ben-Jacob, E., & Jaklevic, R. C. (1989). *Physical Review Letters, 63*, 801–804.
71. Markovich, G., Leff, D. V., Chung, S. W., Soyez, H. M., Dunn, B., & Heath, J. R. (1997). Parallel fabrication and single-electron charging of devices based on ordered, two-dimensional phases of organically functionalized metal nanocrystals. *Applied Physics Letters, 70*, 3107–3109.
72. Wang, B., Xiao, X., Huang, X., Sheng, P., & Hou, J. G. (2000). Single-electron tunneling study of two-dimensional gold clusters. *Applied Physics Letters, 77*, 1179–1181.
73. Klein, D. L., McEuen, P. L., Bowen Katari, J. E., Roth, R., & Alivisatos, A. P. (1996). An approach to electrical studies of single nanocrystals. *Applied Physics Letters, 68*, 2574–2276.
74. Chen, W., Ahmed, H., & Nakazoto, K. (1995). Coulomb blockade at 77 K in nanoscale metallic islands in a lateral nanostructure. *Applied Physics Letters, 66*, 3383–3385.
75. Meirav, U., Kastner, M. A., & Wind, S. J. (1990). Single-electron charging and periodic conductance resonances in GaAs nanostructures. *Physical Review Letters, 65*, 771–774.
76. van Wees, B. J., van Houten, H., Beenakker, C. W. J., Williamson, J. G., Kouwenhoven, L. P., van der Marel, D., & Foxon, C. T. (1988). Quantized conductance of point contacts in a two-dimensional electron gas. *Physical Review Letters, 60*, 848–850.
77. Datta, S. (1997). *Electronic transport in mesoscopic systems*. Cambridge: Cambridge University Press.
78. Lu, W., & Lieber, C. M. (2007). Nanoelectronics from the bottom up. *Nature Materials, 6*, 841–850.
79. Bond, G. C., & Thomson, D. T. (1999). Catalysis by gold. *Catalysis Reviews: Science and Engineering, 41*(3–4), 319–388.
80. Bond, G. C. (2002). Gold: A relatively new catalyst. *Catalysis Today, 72*, 5–9.
81. Bone, W. A., & Wheeler, R. V. (1906). The combination of hydrogen and oxygen in contact with hot surfaces. *Philosophical Transactions of the Royal Society A, 206*, 1–67.
82. Klabunde, K. J., Stark, J. V., Koper, O., Mohs, C., Park, D. G., Decker, S., Jiang, Y., Lagadic, I., & Zhang, D. (1996). Nanocrystals as stoichiometric reagents with unique surface chemistry. *The Journal of Physical Chemistry, 100*, 12142–12153.

83. Sun, C. Q. (2007). Size dependence of nanostructures: Impact of bond order deficiency. *Progress in Solid State Chemistry, 35*, 1–159.

84. Klabunde, K. J., & Richards, R. M. (Eds.). (2009). *Nanoscale materials in chemistry* (2nd ed.). Hoboken: Wiley.

85. Sun, C. Q., Bai, H. L., Li, S., Tay, B. K., & Jiang, E. Y. (2004). Size-effect on the electronic structure and the thermal stability of a gold nanosolid. *Acta Materialia, 52*, 501–505.

86. Sakai, H. (1996). Surface-induced melting of small particles. *Surface Science, 351*, 285–291.

87. Stranski, I. N. (1942). Über das Verhalten nichtpolarer Kristalle dicht unterhalb des Schmelzpunktes und beim Schmelzpunkt selbst. *Zeitschrift für Physik, 119*, 22–34.

88. Frenken, J. W. M., Maree, P. M. J., & Van Der Veen, J. F. (1986). Observation of surface-initiated melting. *Physical Review B, 34*, 7506–7516.

89. Tartaglino, U., Zykova-Timan, T., Ercolessi, F., & Tosatti, E. (2005). Material surfaces and nanosystems close to the melting temperature (Proceedings of the IV International Conference High Temperature Capillarity). *Journal of Materials Science, 40*, 2141–2147.

90. Mei, Q. S., & Lu, K. (2007). Melting and superheating of crystalline solids: From bulk to nanocrystals. *Progress in Materials Science, 52*, 1175–1262.

91. Sang, L. V., Hoang, V. V., & Hang, N. T. T. (2013). Molecular dynamics simulation of melting of fcc Lennard-Jones nanoparticles. *European Physical Journal: D, 67*(64), 1–8.

92. Oxtoby, D. W. (1990). New perspectives on freezing and melting. *Nature, 347*, 725–730.

93. Bischof, J., Scherer, D., Herminghaus, S., & Leiderer, P. (1996). Dewetting modes of thin metallic films: Nucleation of holes and spinodal dewetting. *Physical Review Letters, 77*, 1536–1539.

94. Herminghaus, S., Jacobs, K., Mecke, K., Bischof, J., Fery, A., Ibn-Elhaj, M., & Schlagowski, S. (1998). Spinodal dewetting in liquid crystal and liquid metal films. *Science, 282*, 916–919.

95. Habenicht, A., Olapinski, M., Burmeister, F., Leiderer, P., & Boneberg, J. (2005). Jumping, nanodroplets. *Science, 309*, 2043–2045.

96. Gromov, D. G., & Gavrilov, S. A. (2009). Manifestation of the heterogeneous mechanism upon melting of low-dimensional systems. *Physics of the Solid State, 51*, 2135–2144 and references therein.

97. Wang, Y. T., Teitel, S., & Dellago, C. (2005). Melting of icosahedral gold nanoclusters from molecular dynamics simulations. *The Journal of Chemical Physics, 122*, 214722–214738.

98. Zhao, Y., & Yakobson, B. I. (2003). What is the ground-state structure of the thinnest Si nanowires? *Physical Review Letters, 91*(1–4), 035501.

99. Guisbiers, G., Van Overschelde, O., & Wautelet, M. (2008). Theoretical investigation of size and shape effects on the melting temperature and energy bandgap of TiO_2 nanostructures. *Applied Physics Letters, 92*(1–3), 103121.

100. Dash, J. G. (1999). History of the search for continuous melting. *Reviews of Modern Physics, 71*, 1737–1743 and references therein.

101. Wang, Y., Teitel, S., & Dellago, C. (2004). Melting and equilibrium shape of icosahedral gold nanoparticles. *Chemical Physics Letters, 394*, 257–261.

102. Chattopadhyuy, K., & Goswami, R. (1991). Melting and superheating of metals and alloys. *Progress in Materials Science, 42*, 287–300.

103. Jiang, Q., Zhang, Z., & Li, J. C. (2000). *Acta Materialia, 48*, 4791–4795 and references therein.

104. Shirinyan, A. S., Gusak, A. M., & Wautelet, M. (2005). Melting and superheating of nanowires. *Acta Materialia, 55*, 5025.

105. Saka, H., Nishikawa, Y., & Imura, T. (1988). Melting temperature of In particles embedded in an Al matrix. *Philosophical Magazine A, 57*, 895–906.

106. Thomson, J. J. (1888). *Application of dynamics to physics and chemistry*. London: McMillan.

107. Pawlow, P. (1910). Über den Dampfdruck der Körner einer festen Substanz. *Zeitschrift für Physikalische Chemie, 68*, 316–322.

108. Pawlow, P. N. (1910). Ueber den Einfluss der Oberfläche einer festen Phase auf die latente Wärme und die Temperatur des Schmelzens. *Zeitschrift für Chemie und Industrie der Kolloide, 7*, 37–39.

109. Barybin, A., & Shapovalov, V. (2011). Modification of Pawlow's thermodynamical model for the melting of small single-component particles. *Journal of Applied Physics, 109*(1–9), 034303.

110. Lindemann, F. A. (1910). The calculation of molecular vibration frequencies. *Zeitschrift für Physik, 11*, 609–612.

111. Couchman, R., & Jesser, W. A. (1977). Thermodynamic theory of size dependence of melting temperature in metals. *Nature, 269*, 481–483.

112. Couchman, P. R., & Ryan, C. L. (1978). The Lindmann hypothesis and the size-dependence of melting temperature. *Philosophical Magazine A, 37*, 369–373.

113. Couchman, P. R. (1979). The Lindemann hypothesis and the size dependence of melting temperatures. II. *Philosophical Magazine A, 40*, 637–643.

114. Hoshino, K., & Shimamura, S. (1979). A simple model for the melting of fine particles. *Philosophical Magazine A, 40*, 137–141.

115. Nanda, K. K. (2009). Size-dependent melting of nanoparticles: Hundred years of thermodynamic model. *Pramana, 72*, 617–628.

116. Hanszen, K. J. (1960). Theoretische Untersuchungen über den Schmelzpunkt Ein Beitrag zur Thermodynamik der Grenzflächen. *Zeitschrift für Physik, 157*, 523–553.

117. Beaglehole, D. (1991). Surface melting of small particles, and the effects of surface impurities. *Journal of Crystal Growth, 112*, 663–669.

118. Wautelet, M. (1990). Size effect on the melting (or disordering) temperature of small particles. *Solid State Communications, 74*, 1237–1239.

119. Qi, W. H., Wang, M. P., Zhou, M., Shen, X. Q., & Zhang, X. F. (2006). Modeling cohesive energy and melting temperature of nanocrystals. *Journal of Physics and Chemistry of Solids, 67*, 851–855.

120. Yang, C. C., & Li, S. (2007). Investigation of cohesive energy effects on size-dependent physical and chemical properties of nanocrystals. *Physical Review B, 75*(1–5), 165413.

121. Nanda, K. K., Sahu, S. N., & Behera, S. N. (2002). Liquid-drop model for the size-dependent melting of low-dimensional systems. *Physical Review A, 66*(1–8), 013208.

122. Ercolessi, F., Andreoni, W., & Tosatti, E. (1991). Melting of small gold particles: Mechanism and size effect. *Physical Review Letters, 66*, 911–914.

123. Celestini, F., Pellenq, R. J.-M., Bordarier, P., & Rousseau, B. (1996). Melting of Lennard-Jones clusters in confined geometries. *Zeitschrift für Physik D Atoms, 37*, 49–53.

124. Delogu, F. (2005). Structural and energetic properties of unsupported Cu nanoparticles from room temperature to the melting point: Molecular dynamics simulations. *Physical Review B, 72*, 205418.

125. Alavi, S., & Thompson, D. L. (2006). Molecular dynamics simulation of the melting of aluminum nanoparticles. *The Journal of Physical Chemistry. A, 110*, 1518–1523.

126. Wang, Y., & Dellago, C. (2003). Structural and morphological transitions in gold nanorods: A computer simulation study. *The Journal of Physical Chemistry. B, 107*, 9214–9219.

127. Zhang, Y., Wen, Y.-H., Zheng, J.-C., & Zhu, Z. (2009). Energetic and structural evolution of gold nanowire under heating process: A molecular dynamics study. *Physics Letters A, 373*, 3454–3458.

128. Wen, Y.-H., Zhang, Y., Zheng, J.-C., Zhu, Z.-Z., & Sun, S.-G. (2009). Orientation-dependent structural transition and melting of Au nanowires. *Journal of Physical Chemistry C, 113*(48), 20611–20617.

129. Cross, M. W., & Varhue, W. J. (2008). Radiative melting of crystalline ruthenium oxide nanorods. *Nanotechnology, 19*, 435705 (5 pp).

130. Karabacak, T., DeLuca, J. S., Wang, P.-I., Ten Eyck, G. A., Ye, D., Wang, G., & Lu, T. (2006). Low temperature melting of copper nanorod arrays. *Journal of Applied Physics, 99*(1–6), 064304.

131. Olson, E. A., Yu Efremov, M., Zhang, M., Zhang, Z., & Allen, L. H. (2005). Size-dependent melting of Bi nanoparticles. *Journal of Applied Physics, 97*, 034304 (9 pages).

132. Coombes, C. J. (1972). The melting of small particles of lead and indium. *Journal of Physics F: Metal Physics, 2*, 441–449.

133. Wronski, C. R. M. (1967). The size dependence of the melting point of small particles of tin. *Journal of Applied Physics, 18*, 1731–1737.

134. Wang, P.-I., Lee, S. H., Parker, T. C., Frey, M. D., Karabacak, T., Lu, J.-Q., & Lu, T.-M. (2009). Low temperature wafer bonding by copper nanorod array. *Electrochemical and Solid-State Letters, 124*, H138–H141.

135. Weisbuch, C., & Vinter, B. (2014). *Quantum semiconductor structures: Fundamentals and applications*. Boston: Academic Press.

136. Bastard, G. (1990). *Wave mechanics applied to semiconductor heterostructures*. New York: Wiley.

137. Esaki, L., & Tsu, R. (1970). Superlattice and negative differential conductivity in semiconductors. *IBM Journal of Research and Development, 14*, 61–65.

138. Nag, B. R. (2000). *Physics of quantum well devices*. Dordrecht: Kluwer Academic Publisher.

139. Cho, A. Y. (1991). Advances in molecular beam epitaxy (MBE). *Journal of Crystal Growth, 111*, 1–13.

140. Esaki, L., & Chang, L. L. (1974). New transport phenomenon in a semiconductor superlattice. *Physical Review Letters, 33*, 495–498.

141. Dingle, R., Wiegmann, W., & Henry, C. H. (1974). Quantum states of confined carriers in very thin $Al_xGa_{1-x}As$-GaAs-$Al_xGa_{1-x}As$ heterostructures. *Physical Review Letters, 33*, 827–830.

142. Bastard, G. (1981). Superlattice band structure in the envelope-function approximation. *Physical Review B, 24*, 5693–5697.

143. Bastard, G. (1982). Theoretical investigations of superlattice band structure in the envelope-function approximation. *Physical Review B, 25*, 7584–7597.

144. Altarelli, M. (1986). In G. Allan, G. Bastard, N. Boccara, M. Lannoo, & M. Voods (Eds.), *Heterojunctions and semiconductor superlattices*. Berlin/New York: Springer-Verlag.

145. White, S. R., & Sham, L. J. (1981). Electronic properties of flat-band semiconductor heterostructures. *Physical Review Letters, 47*, 879–882.

146. Weisbuch, C. (1987). Fundamental properties of III-V semiconductor two-dimensional quantized structures: The basis for optical and electronic device applications. In R. Dingle (Ed.), *Semiconductors and Semimetals* (Vol. 24). New York: Academic Press.

147. Dean, P. J. (1977). III–V compound semiconductors. In J. I. Pankove (Ed.), *Electroluminescence* (pp. 63–132). Berlin/Heidelberg: Springer.

148. Nakamura, S., Pearton, S., & Fasol, G. (2000). *The blue laser diode* (2nd ed.). Berlin/Heidelberg: Springer.

149. Bugajski, M., & Reginski, K. (1996). Optical properties of semiconductor quantum wells. *Opto-Electronics Review, 4*, 83–100.

150. Fox, M. (2001). *Optical properties of solids*. Oxford: Clarendon.

151. Ando, T., Fowler, A. D., & Stern, F. (1982). Electronic properties of two-dimensional systems. *Reviews of Modern Physics, 54*, 437–672.

152. Han, J., Crawford, M. H., Shul, R. J., Figiel, J. J., Banas, M., Zhang, L., Song, Y. K., Zhou, H., & Nurmikko, A. V. (1998). AlGaN/GaN quantum well ultraviolet light emitting diodes. *Applied Physics Letters, 73*, 1688–1690.

153. Sturge, M. D. (1962). Optical Absorption of Gallium Arsenide between 0.6 and 2.75 eV. *Physics Review, 127*, 768–773: *Erratum Physics Review, 129*, 2835 (1963).

154. Greene, R. L., Bajaj, K. K., & E: Phelps, D. (1984). Energy levels of Wannier excitons in GaAs $-$ $Ga_{1-x}Al_xAs$ quantum-well structures. *Physical Review B, 29*, 1807–1812.

155. Bastard, G., Mendez, E. E., Chang, L. L., & Esaki, L. (1982). Exciton binding energy in quantum wells. *Physical Review B, 26*, 1974–1979.

156. Shinada, M., & Sugano, S. (1966). Interband optical transitions in extremely anisotropic semiconductors. I. Bound and unbound exciton absorption. *Journal of the Physical Society of Japan, 21*, 1936–1946.

157. Iotti, R. C., & Andreani, L. C. (1997). Crossover from strong to weak confinement for excitons in shallow or narrow quantum wells. *Physical Review B, 56*, 3922–3932.

158. Chemia, D. S., & Miller, D. A. B. (1985). Excitonic nonlinear-optical effects in semiconductor quantum-well structures. *Journal of the Optical Society of America B: Optical Physics, 2*, 1155–1173.
159. Loehr, J. P., & Singh, J. (1990). Nonvariational numerical calculations of excitonic properties in quantum wells in the presence of strain, electric fields, and free carriers. *Physical Review B, 42*, 7154–7162.
160. Miller, R. C., Kleinman, D. A., Nordland, W. A., Jr., & Gossard, A. C. (1980). Luminescence studies of optically pumped quantum wells in GaAs-Al_xGa_{1-x}As multilayer structures. *Physical Review B, 22*, 863–871.
161. Sanders, G. D., & Chang, Y. C. (1985). Optical properties in modulation-doped GaAs-$Ga_{1-x}Al_x$As quantum wells. *Physical Review B, 31*, 6892–6895.
162. Miller, D. A. B., Chemia, D. S., Eilenberger, D. J., Smith, P. W., Gossard, A. C., & Tsang, W. T. (1982). Large room-temperature optical nonlinearity in GaAs/Ga_{1-x} Al_xAs multiple quantum well structures. *Applied Physics Letters, 41*, 679–681.
163. Law, M., Goldberger, J., & Yang, P. (2004). Semiconductor nanowires and nanotubes. *Annual Review of Materials Research, 34*, 83–122. -(first published online as a Review in Advance, 2004 DOI:10.1146/annurev.matsci.34.040203.112300).
164. Petroff, P. M., Gossard, A. C., Logan, R. A., & Wiegmann, W. (1983). Toward quantum well wires: Fabrication and optical properties. *Applied Physics Letters, 41*, 635–637.
165. Stern, M. B., Craighead, H. G., Liao, P. F., & Mankiewich, P. M. (1984). Fabrication of 20-nm structures in GaAs. *Applied Physics Letters, 45*, 410–412.
166. Kash, K., Scherer, A., Worlock, J. M., Craighead, H. G., & Tamargo, M. C. (1986). Optical spectroscopy of ultrasmall structures etched from quantum wells. *Applied Physics Letters, 49*, 1043–1045.
167. Grambow, P., Demel, T., Heitmann, D., Kohl, M., Schiile, R., & Ploog, K. (1989). Preparation of One-Dimensional Single and Multi-Layered quantum wire by ultrafine deep mesa etching techniques. *Microelectronic Engineering, 9*, 357–360.
168. Kohl, M., Heitmann, D., Grambow, P., & Ploog, K. (1989). One-dimensional magneto-excitons in GaAs/Al_xGa_{1-x}As quantum wires. *Physical Review Letters, 63*, 2124–2127.
169. Kapon, E., Tamargo, M. C., & Hwang, D. M. (1987). Molecular beam epitaxy of GaAs/AlGaAs superlattice heterostructures on nonplanar substrates. *Applied Physics Letters, 50*, 347–349.
170. Turco, F. S., Simhony, S., Kash, K., Hwang, D. M., Ravi, T. S., Kapon, E., & Tamargo, M. C. (1990). Molecular beam epitaxial growth of GaAs/AlAs and GaAs/AlGaAs quantum wells on sub-micron-period corrugated substrates. *Journal of Crystal Growth, 104*, 766–772.
171. Hoenk, M. E., Nieh, C. W., Chen, H. Z., & Vahala, K. J. (1989). Compositional modulation in Al_xGa_{1-x}As epilayers grown by molecular beam epitaxy on the (111) facets of grooves in a nonplanar substrate. *Applied Physics Letters, 55*, 53–55.
172. Bhat, R., Kapon, E., Hwang, D. M., Koza, M. A., & Yun, C. P. (1988). Patterned quantum well heterostructures grown by OMCVD on non-planar substrates: Applications to extremely narrow SQW lasers. *Journal of Crystal Growth, 93*, 850–856.
173. Kapon, E., Walther, M., Christen, J., Grundmann, M., Caneau, C., Hwang, D. M., Colas, E., Bhat, R., Song, G. H., & Bimberg, D. (1992). Quantum wire heterostructure for optoelectronic applications. *Superlattices and Microstructures, 12*, 491–499.
174. Kash, K., Bhat, R., Mahoney, D. D., Lin, P. S. D., Scherer, A., Worlock, J. M., Van der Gaag, B. P., Koza, M., & Grabbe, P. (1989). Strain-induced confinement of carriers to quantum wires and dots within an InGaAs-InP quantum well. *Applied Physics Letters, 55*, 681–683.
175. Gershoni, D., Weiner, J. S., Chu, S. N. G., Baraff, G. A., Vandenberg, J. M., Pfeiffer, L. N., West, K., Logan, R. A., & Tanbun-Ek, T. (1990). Optical transitions in quantum wires with strain-induced lateral confinement. *Physical Review Letters, 65*, 1631–1634.
176. Petroff, P. M., Gossard, A. C., & Wiegmann, W. (1984). Structure of AlAs-GaAs interfaces grown on (100) vicinal surfaces by molecular beam epitaxy. *Applied Physics Letters, 45*, 620–623.

177. Pryor, C. (1991). Electronic structure and optical properties of serpentine superlattice quantum-wire arrays. *Physical Review B, 44*, 12912–12917.
178. Rossi, F., & Molinari, E. (1996). Linear and nonlinear optical properties of realistic quantum-wire structures: The dominant role of Coulomb correlation. *Physical Review B, 53*, 16462–16473.
179. Chang, K., & Xia, J. B. (1998). Quantum-confined Stark effects of exciton states in V-shaped GaAs/Al$_x$Ga$_{1-x}$As quantum wires. *Physical Review B, 58*, 2031–2037.
180. Bockelmann, U., & Bastard, G. (1991). Interband optical transitions in semiconductor quantum wires: Selection rules and absorption spectra. *Europhysics Letters, 15*, 215–220.
181. Suemune, I., & Coldren, L. A. (1988). Band-mixing effects and excitonic optical properties in GaAs quantum wire structures-comparison with the quantum wells. *IEEE Journal of Quantum Electronics, QE-24*, 1778–1790.
182. Einevoll, G. T., & Chang, Y. C. (1989). Effective bond-orbital model for acceptor states in semiconductors and quantum dots. *Physical Review B, 40*, 9683–9697.
183. Citrin, D. S., & Chang, Y. C. (1990). Subband structures of semiconductor quantum wires from the effective-bond orbital model. *Journal of Applied Physics, 68*, 161–168.
184. Citrin, D. S., & Chang, Y. C. (1991). Theory of optical anisotropy in quantum-well-wire arrays with two-dimensional quantum confinement. *Physical Review B, 43*, 11703–11719.
185. McIntyre, C. R., & Sham, L. H. (1992). Theory of luminescence polarization anisotropy in quantum wires. *Physical Review B, 45*, 9443–9446.
186. Sercel, P. C., & Vahala, K. J. (1990). Analytical technique for determining the polarization dependence of optical matrix elements in quantum wires with band-coupling effects or determining the polarization dependence of optical matrix elements in quantum wires with band-coupling effects. *Applied Physics Letters, 57*, 545–547.
187. Sercel, P. C., & Vahala, K. J. (1991). Polarization dependence of optical absorption and emission in quantum wires. *Physical Review B, 44*, 5681–5691.
188. Oberli, D. Y., Vouilloz, F., Dupertuis, M.-A., Fall, C., & Kapon, E. (1995). Optical spectroscopy of semiconductor quantum wires. *Il Nuovo Cimento D, 17*(11–12), 1641–1650.
189. Nagamune, Y., Arakawa, Y., Tsukamoto, S., Nishioka, M., Sasaki, S., & Miura, N. (1992). Photoluminescence spectra and anisotropic energy shift of GaAs quantum wires in high magnetic fields. *Physical Review Letters, 69*, 2963–2966.
190. Wegscheider, W., Pfeiffer, L. N., Dignam, M. M., Pinczuk, A., West, K. W., McCall, S. L., & Hull, R. (1993). Lasing from excitons in quantum wires. *Physical Review Letters, 71*, 4071–4074.
191. Rinaldi, R., Cingolani, R., Lepore, M., Ferrara, M., Catalano, I. M., Rossi, F., Rota, L., Molinari, E., Lugli, P., Marti, U., Martin, D., Morier-Gemoud, F., Ruterana, P., & Reinhart, F. K. (1994). Exciton binding energy in GaAs V-shaped quantum wires. *Physical Review Letters, 73*, 2899–2902.
192. Someya, T., Akiyama, H., & Sakaki, H. (1995). Laterally squeezed excitonic wave function in quantum wires. *Physical Review Letters, 74*, 3664–3666.
193. Someya, T., Akiyama, H., & Sakaki, H. (1996). Enhanced binding energy of one-dimensional excitons in quantum wires. *Physical Review Letters, 76*, 2965–2967.
194. Weman, H., Potemski, M., Lazzouni, M. E., Miller, M. S., & Merz, J. L. (1996). Magneto-optical determination of exciton binding energies in quantum-wire superlattices. *Physical Review B, 53*, 6959–6962 and references therein.
195. Loudon, R. (1959). One-dimensional hydrogen atom. *American Journal of Physics, 27*, 649–655.
196. Elliot, R. J., & Loudon, R. (1959). Theory of fine structure on the absorption edge in semiconductors. *Journal of Physics and Chemistry of Solids, 8*, 382–388.
197. Elliot, R. J., & Loudon, R. (1960). Theory of the absorption edge in semiconductors in a high magnetic field. *Journal of Physics and Chemistry of Solids, 15*, 196–207.
198. Ogawa, T., & Takagahara, T. (1991). Interband absorption spectra and Sommerfeld factors of a one-dimensional electron-hole system. *Physical Review B, 43*, 14325–14328.

199. Ogawa, T., & Takagahara, T. (1991). Optical absorption and Sommerfeld factors of one-dimensional semiconductors: An exact treatment of excitonic effects. *Physical Review B, 44*, 8138–8156.
200. Chang, Y. C., Chang, L. L., & Esaki, L. (1985). A new one-dimensional quantum well structure. *Applied Physics Letters, 47*, 1324–1326.
201. Rossi, F., Goldoni, G., & Molinari, E. (1997). Shape-independent scaling of excitonic confinement in realistic quantum wires. *Physical Review Letters, 78*, 3527–3530.
202. Lage, H., Heitmann, D., Cingolani, R., Granbow, P., & Ploog, K. (1991). Center-of-mass quantization of excitons in GaAs quantum-well wires. *Physical Review B, 44*, 6550–6553.
203. Rinaldi, R., Cingolani, R., Ferrara, M., Lage, H., Teitmann, D., & Ploog, K. (1992). Emission properties of quantum-well wires under stationary conditions. *Physical Review B, 47*, 7275.
204. Kapon, E., Hwang, D. M., & Bhat, R. (1989). Stimulated emission in semiconductor quantum wire heterostructures. *Physical Review Letters, 63*, 430–433.
205. Bimberg, D., Grundmann, M., & Ledentsov, N. N. (1998). *Quantum dot heterostructures*. Chichester: Wiley.
206. Walter, P., Welcomme, E., Hallegot, P., Zaluzec, N. J., Deeb, C., Castaing, J., Veyssiere, P., Breniaux, R., Leveque, J. L., & Tsoucaris, G. (2006). Early use of PbS nanotechnology for an ancient hair dyeing formula. *Nano Letters, 6*, 2215–2219.
207. Onushchenko, A. A. (1981). Quantum size effect in 3-dimensional microscopic semiconductor crystals. *JETP Letters, 34*, 345–349.
208. Efros, A. L. (1982). Interband absorption of light in a semiconductor sphere. *Soviet Physics – Semiconductors, 16*, 772–775.
209. Rossetti, R., Ellison, J. L., Gibson, J. M., & Brus, L. E. (1984). Size effects in the excited electronic states of small colloidal CdS crystallites. *The Journal of Chemical Physics, 80*, 4464–4469.
210. Yoffe, A. D. (2001). Semiconductor quantum dots and related systems: Electronic, optical, luminescence and related properties of low dimensional systems. *Advances in Physics, 50*, 1–208.
211. Bryan, J. D., & Gamelin, D. R. (2005). Doped semiconductor nanocrystals: Synthesis, characterization, physical properties, and applications. *Progress in Inorganic Chemistry, 54*, 47–126.
212. Jiang, W. H., Xu, H. Z., Xu, B., Ye, X. L., Wu, J., Ding, D., Liang, J. B., & Wang, Z. G. (2000). Annealing effect on the surface morphology and photoluminescence of InGaAs/GaAs quantum dots grown by molecular beam epitaxy. *Journal of Crystal Growth, 212*, 356–359.
213. Sellin, R. L., Ribbat, C., Grundmann, M., Ledentsov, N. N., & Bimberg, D. (2001). Close-to-ideal device characteristics of high-power InGaAs/GaAs quantum dot lasers. *Applied Physics Letters, 78*, 1207–1209.
214. Tsatsulnikov, A. F., Kovsh, A. R., Zhukov, A. E., Shernyakov, Y. M., Musikhin, Y. G., Ustinov, V. M., Bert, N. A., Kopev, P. S., Alferov, Z. I., Mintairov, A. M., Merz, J. L., Ledentsov, N. N., & Bimberg, D. (2000). Volmer–Weber and Stranski–Krastanov InAs-(Al,Ga) As quantum dots emitting at 1.3 μm. *Journal of Applied Physics, 88*, 6272–6275.
215. Ledentsov, N. N., Shchukin, V. A., Grundmann, M., Kirstaedter, N., Böhrer, J., Schmidt, O., Bimberg, D., Ustinov, V. M., Egorov, A. Y., Zhukov, A. E., Kopev, P. S., Zaitsev, S. V., Gordeev, N. Y., Alferov, Z. I., Borovkov, A. I., Kosogov, A. O., Ruvimov, S. S., Werner, P., Gosele, U., & Heydenreich, J. (1996). Direct formation of vertically coupled quantum dots in Stranski-Krastanow growth. *Physical Review B, 54*, 8743–8750.
216. Xia, Y., Xia, X., & Peng, H.-C. (2015). Shape-controlled synthesis of colloidal metal nanocrystals: Thermodynamic versus kinetic products. *Journal of the American Chemical Society, 137*, 7947–7966.
217. Overbeek, J. T. G. (1982). Monodisperse colloidal systems, fascinating and useful. *Advances in Colloid and Interface Science, 15*, 251–277.
218. Reed, M. A., Randall, J. N., Aggarwal, R. J., Matyi, R. J., Moore, T. M., & Wetsel, A. E. (1988). Observation of discrete electronic states in a zero-dimensional semiconductor nanostructure. *Physical Review Letters, 60*, 535–537.

219. Alivisatos, A. P. (1996). Semiconductor clusters, nanocrystals, and quantum dots. *Science, 271*, 933–937.
220. Banin, U., Bruchez, M., Alivisatos, A. P., Ha, T., Weiss, S., & Chemla, D. S. (1999). Evidence for a thermal contribution to emission intermittency in single CdSe/CdS core/shell nanocrystals. *The Journal of Chemical Physics, 110*, 1195–1201.
221. Empedocles, S. A., Neuhauser, R., Shimizu, K., & Bawendi, M. G. (1999). Photoluminescence from single semiconductor nanostructures. *Advanced Materials, 11*, 1243–1256.
222. Chavez-Pirson, A., Temmyo, J., Kamada, H., Gotoh, H., & Ando, H. (1998). Near-field optical spectroscopy and imaging of single InGaAs/AlGaAs quantum dots. *Applied Physics Letters, 72*, 3494–3496.
223. Nirmal, M., Dabbousi, B. O., Bawendi, M. G., Macklin, J. J., Trautman, J. K., Harris, T. D., & Brus, L. E. (1996). Fluorescence intermittency in single cadmium selenide nanocrystals. *Nature, 383*, 802–804.
224. Nötzel, R., Niu, Z., Ramsteiner, M., Schönherr, H.-P., Tranpert, A., Däweritz, L., & Ploog, K. H. (1998). Uniform quantum-dot arrays formed by natural self-faceting on patterned substrates. *Nature, 392*, 56–59.
225. Tersoff, J., Teichert, C., & Lagally, M. G. (1996). Self-organization in growth of quantum dot superlattices. *Physical Review Letters, 76*, 1675–1678.
226. Gammon, D., Snow, E. S., Shanabrook, B. V., Katzer, D. S., & Park, D. (1996). Homogeneous linewidths in the optical spectrum of a single Gallium Arsenide Quantum Dot. *Science, 273*, 87–90.
227. Brus, L. E. (1986). Electronic wave functions in semiconductor clusters: Experiment and theory. *The Journal of Physical Chemisty, 90*(12), 2555–2560; Brus, L. E. (1984). Electron–electron and electronhole interactions in small semiconductor crystallites: The size dependence of the lowest excited electronic state. *The Journal of Chemical Physics, 80*, 4403–4409.
228. Ronda, C. R. (2008). In R. Ronda (Ed.), *Luminescence: From theory to applications*. Weinheim: Wiley-VCH Verlag GmbH&Co.KGaA.
229. Hartmann, A., Ducommun, Y., Kapon, E., Hohenester, U., & Molinari, E. (2000). Few-particle effects in semiconductor quantum dots: Observation of multicharged excitons. *Physical Review Letters, 84*, 5648–5651.
230. Warburton, R. J., Schaflein, C., Haft, D., Bickel, F., Lorke, A., Karrai, K., Garcia, J. M., Schoenfeld, W., & Petroff, P. M. (2000). Optical emission from a charge-tunable quantum ring. *Nature, 405*, 926–929.
231. Finley, J. J., Ashmore, A. D., Lemaître, A., Mowbray, D. J., Skolnick, M. S., Itskevich, I. E., Maksym, P. A., Hopkinson, M., & Krauss, T. F. (2001). Charged and neutral exciton complexes in individual self-assembled In (Ga) As quantum dots. *Physical Review B, 63*, 073307–073310.
232. Findeis, F., Baier, M., Zrenner, A., Bichler, M., Abstreiter, G., Hohenester, U., & Molinari, E. (2001). Optical excitations of a self-assembled artificial ion. *Physics Review, 63*(1–4), 121309.
233. Alivisatos, A. P. (1996). Perspectives on the physical chemistry of semiconductor nanocrystals. *The Journal of Physical Chemistry, 100*, 13226–13239.
234. Wang, Y., & Herron, N. (1991). Nanometer-sized semiconductor clusters–materials synthesis, quantum size effects, and photophysical properties. *The Journal of Physical Chemistry, 95*, 525–532.
235. Bang, J., Yang, H., & Holloway, P. H. (2006). Enhanced and stable green emission of ZnO nanoparticles by surface segregation of Mg. *Nanotechnology, 17*, 973–978.
236. Ma, Y., Wang, X., Jia, Y., Chen, X., Han, H., & Li, C. (2014). Titanium dioxide-based nanomaterials for photocatalytic fuel generations. *Chemical Reviews, 114*, 9987–10043.
237. Kamat, P. V. (2014). Quantum dot solar cells. Semiconductor nanocrystals as light harvesters. *Journal of Physical Chemistry C, 112*, 18737–18753.
238. Homola, J., Yeea, S. S., & Gauglitzb, G. (1999). Surface plasmon resonance sensors: Review. *Sensors and Actuators B: Chemical, 54*, 3–15.

239. Mie, G. (1908). Beiträge zur optik trüber medien, speziell kolloidaler metallösungen. *Annalen der Physik, 330*, 377–445.

240. Kelly, K. L., Coronado, E., Zhao, L. L., & Schatz, G. C. (2003). The optical properties of metal nanoparticles: The influence of size, shape, and dielectric environment. *The Journal of Physical Chemistry. B, 107*, 668–677.

241. Sosa, I. O., Noguez, C., & Barrera, R. C. (2003). Optical properties of metal nanoparticles with arbitrary shapes. *The Journal of Physical Chemistry. B, 107*, 6269–6275.

242. Dabbousi, B. O., Rodriguez-Viejo, J., Mikulec, F. V., Heine, J. R., Mattoussi, H., Ober, R., Jensen, K. F., & Bawendi, M. G. (1997). (CdSe) ZnS core – shell quantum dots: Synthesis and characterization of a size series of highly luminescent nanocrystallites. *The Journal of Physical Chemistry. B, 101*, 9463–9475.

243. Anker, J. N., Paige Hall, W., Lyandres, O., Shah, N. C., Zhao, J., & Van Duyne, R. P. (2008). Biosensing with plasmonic nanosensors. *Nature Materials, 7*, 442–453.

244. Haes, A. J., & Van Duyne, R. P. (2002). A nanoscale optical biosensor: Sensitivity and selectivity of an approach based on the localized surface plasmon resonance of triangular silver nanoparticles. *Journal of the American Chemical Society, 124*, 10596–10604.

245. Jung, L. S., Campbell, C. T., Chinowsky, T. M., Mar, M. N., & Yee, S. S. (1998). Quantitative interpretation of the response of surface plasmon resonance sensors to adsorbed films. *Langmuir, 14*, 5636–5648.

246. Oldenburg, S. J., Averitt, R. D., Westcott, S. L., & Halas, N. J. (1998). Nanoengineering of optical resonances. *Chemical Physics Letters, 288*, 243–247.

247. Ma, Y., Zhou, J., Zou, W., Jia, Z., Petti, L., & Mormile, P. (2014). Localized surface plasmon resonance and surface enhanced Raman scattering responces of Au@Ag core-shall nanorods with different thickness of Ag shell. *Journal of Nanoscience and Nanotechnology, 14*, 4245–4250.

248. Csapo, E., Oszko, A., Varga, E., et al. (2012). Synthesis and characterization of Ag/Au alloy and core (Ag)-shell(Au) nanoparticles. *Colloids and Surfaces A, Physicochemical and Enginnering Aspects, 415*, 281–287.

249. El-Brolossy, T. A., Abdallah, T., Mohamed, M. B., et al. (2008). Shape and size dependence on the surface plasmon resonance of gold nanoparticles studied by photoacoustic techniques. *The European Physical Journal: Special Topics, 153*, 361–364.

250. Ringe, E., Zhang, J., Langille, M. R., et al. (2010). Effect of size, shape, composition, and support film on localized surface plasmon resonance frequency: A single particle approach applied to silver bipyramids and gold and silver nanocubes. In *Proceedings of the material research society fall meeting*, 1208.

251. Moskovits, M. (2005). Surface enhanced Raman spectroscopy: A brief retrospective. *Journal of Raman Spectroscopy, 36*, 485–496.

252. Moore, C. B., Rison, W., Mathis, J., & Aulich, G. (2000). Lightning rod improvement studies. *Journal of Applied Meteorology, 39*, 593–609.

253. Lee, J., Hua, B., Park, S., et al. (2014). Tailoring surface plasmons of high-density gold nanostar assemblies on metal films for surface-enhanced Raman spectroscopy. *Nanoscale, 6*, 616–623.